Resilience through diversity: Lost neuronal heterogeneity in human epilepsy renders networks vulnerable to synchronous transitions

Scott Rich[a,1], **Homeira Moradi Chameh**[a], **Jeremie Lefebvre**[a,b,c,2], **and Taufik A Valiante**[a,d,e,f,g,2]

[a]Krembil Research Institute, University Health Network (UHN), Division of Clinical and Computational Neuroscience, Toronto, Ontario, Canada; [b]University of Ottawa, Department of Biology, Ottawa, Ontario, Canada; [c]University of Toronto, Department of Mathematics, Toronto, Ontario, Canada; [d]University of Toronto, Institute of Biomedical Engineering, Toronto, ON, Canada; [e]University of Toronto, Electrical and Computer Engineering, Toronto, ON, Canada; [f]University of Toronto, Institute of Medical Science, Toronto, ON, Canada; [g]University of Toronto, Division of Neurosurgery, Department of Surgery, Toronto, ON, Canada

This manuscript was compiled on August 20, 2021

A myriad of pathological changes associated with epilepsy, including the loss of specific cell types, improper ion channel expression, and synaptic sprouting, can all be recast as decreases in cell and circuit heterogeneity. We thus propose that epileptogenesis can be recontextualized as a process where reduction in cellular heterogeneity renders neural circuits less resilient to transitions into information-poor, over-correlated seizure states. We provide *in vitro*, *in silico*, and mathematical support for this hypothesis. By comparing patch clamp recordings from human layer 5 (L5) cortical neurons from epileptogenic frontal lobe (from patients with epilepsy) to non-epileptogenic temporal lobe (from patients with epilepsy) and non-epileptogenic frontal lobe (obtained during tumor resection), we demonstrate significantly decreased biophysical heterogeneity of excitatory neurons in seizure generating areas (epilepetogenic zone). When implemented computationally, this experimentally observed decrease in heterogeneity renders model neural circuits prone to sudden dynamical transitions into synchronous states with increased firing activity, paralleling ictogenesis. Computational analysis of reduced neural heterogeneity also explains the surprising experimental finding of significantly decreased excitability in the population activation functions (i.e., FI curves) of neurons from epileptogenic tissue. Mathematical analyses based in mean-field theory reveal clear distinctions in the dynamical structure of networks with low and high heterogeneity, including the presence of multi-stability and saddle-node bifurcations only in networks with the lowest heterogeneity. Taken together, this work provides experimental, computational, and mathematical support for the theory that ictogenic dynamics accompany a reduction in biophysical heterogeneity.

Epilepsy | Seizure | Neural oscillations | Neural heterogeneity | Computational neuroscience

Epilepsy, the most common serious neurological disorder in the world (1), is characterized by the brain's proclivity for seizures, which exhibit highly correlated electrophysiological activity and elevated neuronal spiking (2). While the etiologies that predispose the brain to epilepsy are myriad (3), the dynamics appear to be relatively conserved (4, 5), suggesting a small palette of candidate routes to the seizure state. One potential route to ictogenesis is disruption of excitatory/inhibitory balance (EIB) - a possible "final common pathway" for various epileptogenic etiologies, and a fundamental motivation for decades of basic science research into epilepto- and ictogenesis (6, 7). A disrupted EIB can result in the loss of resilience of neural circuits to correlated inputs (8), a paramount characteristic of ictogenesis. In addition to EIB, biophysical heterogeneity also provides resilience to correlated inputs (9). Thus, EIB can be considered a synaptic mechanism for input decorrelation, while biophysical heterogeneity contributes to decorrelation post-synaptically.

Cellular heterogeneity is the norm in biological systems (10, 11). In the brain, experimental and theoretical work has demonstrated that such variability expands the informational content of neural circuits, in part by reducing correlated neuronal activity (12, 13). Since heightened levels of firing and firing rate correlations hallmark seizures (4, 14), we hypothesize that epilepsy may be likened, in part, to pathological reductions in biological heterogeneity which impair decorrelation, and thus circuit resilience to information poor (15), high-firing (2), and highly-correlated states (14).

A number of pathological changes accompanying epileptogenesis can be recast as decreases in biological heterogeneity. Losses of specific cell-types homogenize neural populations (16, 17), down- or upregulation of ion channels in acquired and genetic epilepsies homogenize biophysical properties (18–20), and synaptic sprouting homogenizes neural inputs (21). This recontextualizes epileptogenesis as a process associated with the progressive loss of biophysical heterogeneity.

To explore this hypothesis we combine electrophysiological recordings from human cortical tissue, computational mod-

Significance Statement

Facilitated by access to live human cortical tissue from both healthy and seizure-producing areas, this work explores the role of neuronal biophysical heterogeneity in epilepsy. Experimental characterization of the intrinsic properties of human neurons reveals that this heterogeneity is decreased in seizure-producing brain regions, and that this is associated with a surprising decrease in the excitability of individual neurons. Computational and mathematical analyses show that decreased heterogeneity renders neural circuits more vulnerable to seizure-like dynamics and explains how lost heterogeneity is inherently coupled with the observed changes in neural excitability. This work thus presents a new perspective on the development of epilepsy with experimental, computational, and theoretical support.

Conception and design: SR, HMC, JL, TAV. Experimental data collection: HMC. Data analysis and interpretation: SR, HMC, TAV. Simulations: SR. Mathematical analysis: SR, JL. Initial drafting: SR. Edits and revisions: SR, HMC, JL, TAV. All authors approved the version to be submitted.

The authors have declared that no conflict of interest exists.

[2]J.L. and T.A.V share senior authorship of this work.

[1]To whom correspondence should be addressed. E-mail: scott.rich@uhnresearch.ca

DRAFT

eling, and mathematical analysis to detail the existence and subsequent consequences of one type of reduction in biological variability in epilepsy: the decrease of intrinsic neuronal heterogeneity. We first provide experimental evidence for decreased biophysical heterogeneity in neurons within brain regions that generate seizures (epileptogenic zone) when compared to non-epileptogenic regions. This data constrains an exploration of the effects of heterogeneity in neural excitability on simulated brain circuits. Using a cortical excitatory-inhibitory (E-I) spiking neural network, we show that networks with neuronal heterogeneity mirroring epileptogenic tissue are more vulnerable to sudden shifts from an asynchronous to a synchronous state, which has clear parallels with seizure onset. Networks with neuronal heterogeneity mirroring non-epileptogenic tissue are more resilient to such transitions. These differing heterogeneity levels also underlie significant, yet counter-intuitive, differences in neural activation functions (i.e., frequency-current or FI curves) measured inside and outside the epileptogenic zone. Using mean-field analysis, we show that differences in the predisposition towards a sudden onset of synchrony and activation functions are both consequences of varying degrees of neuronal diversity. Viewed together, our experimental, computational, and mathematical results strongly support the hypothesis that biophysical heterogeneity enhances the dynamical resilience of neural networks while explaining how reduced diversity can predispose circuits to seizure initiation.

Results

Intrinsic biophysical heterogeneity is reduced in human epileptogenic cortex. In search of experimental evidence for reduced biophysical heterogeneity in epileptogenic brain regions, we utilized the rare access to live human cortical tissue obtained during resective surgery. Whole-cell current clamp recordings characterized the passive and active properties of layer 5 (L5) cortical pyramidal cells from these samples, a cell type we have shown to display notable biophysical heterogeneity (22). Biophysical properties of neurons from epileptogenic frontal lobe cortex were contrasted to frontal lobe neurons of patients with no previous history of seizures undergoing tumor resection. Additionally, we obtained recordings from neurons in non-epileptogenic middle temporal gyrus (MTG) from patients with mesial temporal sclerosis, which is the overlying cortex routinely removed to approach deep temporal structures. The MTG is a well-characterized part of the human brain, representing a common anatomical region from which non-epileptogenic brain tissue has been studied electrophysiologically and transcriptomically (22–25), and thus our primary source of non-epileptogenic neurons.

Our analysis concentrated on two characterizations of cellular excitability. The first was the distance to threshold (DTT) measured as the difference between the resting membrane potential (RMP) and threshold voltage (see Supplementary Figure S1 for the distributions of the RMP and threshold voltage along with other electrophysiological details from these samples). Whole-cell recordings revealed less DTT variability (smaller coefficient of variation (CV); p=0.04; two sample coefficient of variation test) in epileptogenic frontal lobe (n=13, CV=20.3%) as compared to non-epileptogenic MTG (n=77, CV=37.1%). A significant difference (smaller CV; p=0.03; two sample coefficient of variation test) was also seen when comparing epileptogenic frontal lobe to non-epileptogenic frontal lobe (n=12, CV=40.8%). Meanwhile, the CVs were not significantly different when comparing non-epileptogenic MTG and non-epileptogenic frontal lobe (p=0.7; two sample coefficient of variation test). These features are more easily appreciated from the Gaussian fits of this data presented in Figure 1**(b)**; all three data sets were deemed normal after passing both the Shapiro-Wilk and D'Agostino & Pearson omnibus normality tests with alpha=0.05. These experimental results imply that the decrease in biophysical heterogeneity observed in epileptogenic cortex was not confounded by sampling from the temporal versus frontal lobe.

While our non-epileptogenic MTG population is notably larger, this is unavoidable given the availability of human cortical tissue (see Discussion). Statistical tests accounting for unequal population sizes were used. Additionally, the significant difference between the standard deviations (SDs) of the DTTs in non-epileptogenic MTG and epileptogenic frontal lobe (p=0.03, Cohen's d effect size=0.5; F-test; SD=7.8 mV in non-epileptogenic MTG and SD=4.4 mV in epileptogenic frontal lobe) that is implemented in our models has a "moderate" effect size. Combined with the fact that statistically significant differences in CVs are seen both in comparing populations with different and similar sizes, we are confident that our statistical comparisons accurately reveal differences between epileptogenic and non-epileptogenic human neurons.

Our second quantification of cellular excitability was the FI curve (i.e., activation function), which captures the firing rate (F) as function of input current (I). The activation function of the population of neurons from the epileptogenic zone displayed qualitative and quantitative differences compared to neurons from non-epileptogenic cortex, be it from MTG or frontal lobe (Figure 1**(c)**). Surprisingly, firing threshold was found to be higher in the epileptogenic zone compared to both non-epileptogenic populations. Additionally, firing rates were significantly lower in the epileptogenic zone (p=0.03 when comparing epileptogenic frontal lobe to non-epileptogenic frontal lobe at 200 pA, p=0.02 when comparing epileptogenic frontal lobe to non-epileptogenic frontal lobe at 250 pA, p=0.009 when comparing epileptogenic frontal lobe to non-epileptogenic MTG at 200 pA, and p=0.002 when comparing epileptogenic frontal lobe to non-epileptogenic MTG at 250 pA; two-way ANOVA-Tukey's multiple comparison test), indicating larger inputs are required to induce high-frequency repetitive firing in individual neurons from epileptogenic tissue. This non-linear behavior is in strong contrast to the activation functions measured in non-epileptogenic zones, characterized by both higher and more linear changes in firing rates. All three populations showed low levels of spike frequency adaptation (Figure 1**(d)**), strongly indicating that these differences are not due to differing adaptation rates. Example firing traces from each population are found in Figure 1**(e)**. This increased excitability of the non-epileptogenic populations appears contradictory to the understanding of seizure as a hyperactive brain state, although some prior studies have hinted at this phenomenon (26, 27). We further investigate this finding in the context of biophysical heterogeneity in the following.

Spiking E-I neural networks with epileptogenic levels of excitatory heterogeneity are more vulnerable to sudden changes in synchrony. Given these confirmatory experimental results, we next explored the effects of biophysical heterogeneity on the transition to a synchronous state akin to the transition to

DRAFT

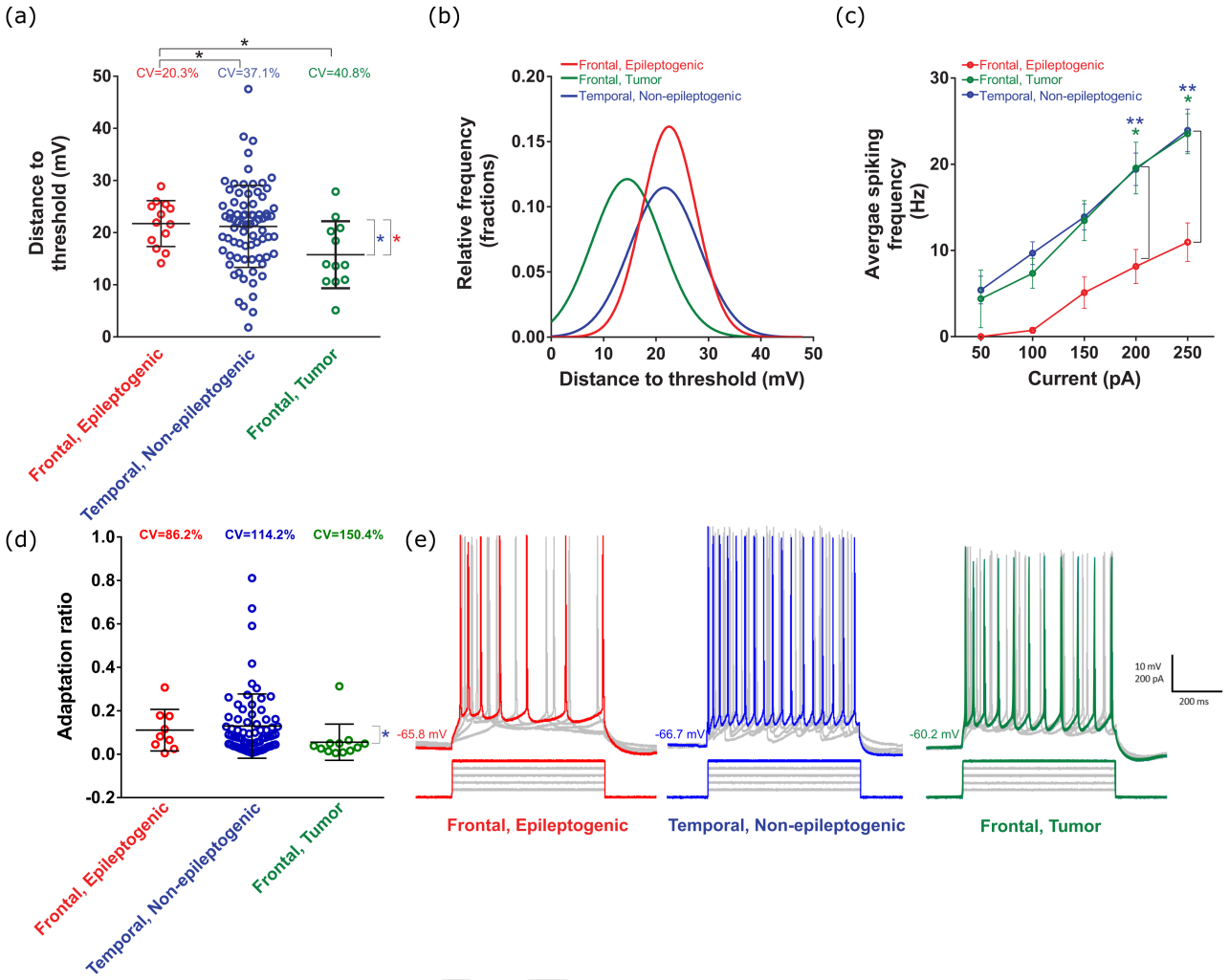

Fig. 1. ***In vitro*** **human tissue recordings reveal significantly different electrophysiological heterogeneity between epileptogenic and non-epileptogenic populations**. **(a)**: The coefficient of variation (CV) in the distance to threshold (DTT) is significantly larger in both the temporal, non-epileptogenic (i.e., non-epileptogenic MTG; n=77) and frontal, tumor (i.e., non-epileptogenic frontal lobe; n=12) populations compared to the frontal, epileptogenic (i.e., epileptogenic frontal lobe; n=13) population (p=0.04 to temporal, non-epileptogenic, p=0.03 to frontal, tumor; two sample coefficient of variation test). The CV measure is implemented considering the significantly reduced mean DTT in frontal, tumor data compared to the other two populations (p=0.01 for both comparisons; non-parametric Mann-Whitney test). We compare the frontal, epileptogenic and temporal, non-epileptogenic populations computationally given their similar mean DTT (p=0.7; non-parametric Mann-Whitney test). Plotted bars indicate mean $\pm$ standard deviation (SD). **(b)**: An alternative visualization of the DTT distributions via fit Gaussian probability density functions. All three data sets were deemed normal after passing both the Shapiro-Wilk and D'Agostino & Pearson omnibus normality test with alpha=0.05. **(c)**: Neurons from non-epileptogenic populations show similar, linear activation functions (i.e., FI curves). There are significant differences between the firing frequencies for a 200 pA injection between frontal, epileptogenic and temporal, non-epileptogenic data (p=0.009; two-way ANOVA-Tukey's multiple comparison test) and between frontal, epileptogenic and frontal, tumor data (p=0.03; two-way ANOVA-Tukey's multiple comparison test), as well as for a 250 pA injection between frontal, epileptogenic and temporal, non-epileptogenic data (p=0.002; two-way ANOVA-Tukey's multiple comparison test) and between frontal, epileptogenic and frontal, tumor data (p=0.02; two-way ANOVA-Tukey's multiple comparison test). Plotted bars indicate mean $\pm$ standard error measure (SEM). **(d)**: All three populations show low levels of spike frequency adaptation, with the only significant difference being between the means from the frontal, tumor and temporal, non-epileptogenic populations (p=0.01; One-Way ANOVA post hoc with Dunn's multiple comparison test). Plotted bars indicate mean $\pm$ SD. **(e)**: Example cell voltage responses following depolarizing current injections (50-250 pA) from all three populations (colors denote population as in previous panels).

seizure (14). We developed a spiking network model of a cortical microcircuit comprised of recurrently connected excitatory and inhibitory neurons (see details in Methods), motivated in part by the long history of seizure modeling (4, 28) and previous models of decorrelated activity in the cortex (8, 29, 30). Our choice of model parameters (see details in Methods) positioned the system near a tipping point at which synchronous activity might arise (31–34) in order to determine the effects of cellular heterogeneity on this potential transition.

We subjected these networks to a slowly linearly increasing external drive to the excitatory cells. This allowed us to observe the dynamics and stability of the asynchronous state, known to be the physiological state of the cortex (8, 29, 30), by determining how vulnerable the network is to a bifurcation forcing the system out of this dynamic and into a state of increased synchrony and firing. A biological analogue for this paradigm would be an examination of whether induced hyper-excitability might drive the onset of seizure-like activity *in vitro*, although such perturbations can more easily be performed continuously (i.e., our linearly increasing external drive) rather than discretely (i.e., inducing hyper-excitability pharmacologically) *in silico*.

To facilitate implementing experimentally-derived heterogeneities in our model, we compared epileptogenic frontal lobe with non-epileptogenic MTG given their similar mean DTT values (p=0.7, non-parametric Mann-Whitney test; mean=21.2 mV for non-epileptogenic MTG and mean=21.7 mV for epileptogenic frontal lobe). These populations display significantly different SDs in their DTT values (reported above). Given the definition of our neuron model (rheobases sampled from a normal distribution with with mean 0, see details in Methods), we implement differing heterogeneities by sampling rheobase values for our neural populations from Gaussian distributions with these varying SDs. In this model, the term rheobase refers to the inflexion point of the model neuron activation function (see Methods). Heterogeneity in this mathematically-defined rheobase is the *in silico* analogue of heterogeneity in the DTT (i.e., the distribution of rheobases in Figure 2**(c-d)** corresponds to a horizontal shift to a mean of 0 of the DTT distributions in Figure 1**(b)**).

The rheobase heterogeneity was parameterized by the SD σ_e for excitatory neurons and σ_i for inhibitory neurons (see diagrams in Figure 2**(a-b)**). This results in diversity in the neurons' activation functions and aligns the variability in their excitabilities with that measured experimentally. We refer to such rheobase heterogeneity simply as heterogeneity in the remainder of the text. Models with epileptogenic (high $\sigma_e = 7.8$ mV, Figure 2**(e)**) and non-epileptogenic (low $\sigma_e = 4.4$ mV, Figure 2**(f)**) excitatory heterogeneity with identical, moderate inhibitory heterogeneity ($\sigma_i = 10.0$ mV) exhibit distinct behaviors. With low excitatory heterogeneity, a sharp increase in excitatory synchrony associated with increased firing rates is observed. In contrast, when the excitatory heterogeneity was high, both synchrony and firing rates scaled linearly with input amplitude.

We further investigated the respective roles of excitatory versus inhibitory heterogeneity in generating these sudden transitions. With non-epileptogenic amounts of excitatory heterogeneity (high σ_e), increases in excitatory synchrony, excitatory firing rates, and inhibitory firing rates were all largely linear regardless of whether σ_i was low (Figure 3**(a)**) or high (Figure 3**(b)**). Conversely, with excitatory heterogeneity reflective of epileptogenic cortex (low σ_e), synchronous transitions were observed for both low (Figure 3**(c)**) and high (Figure 3**(d)**) levels of σ_i. This transition is of notably higher amplitude when σ_i is low, indicative of differing underlying dynamical structures.

Dynamical differences in networks with varying levels of heterogeneity are explained by their distinct mathematical structures. To gain deeper insight into the effect of heterogeneity at a potential transition to synchrony, we derived and analyzed mathematically the mean-field equations associated with our network model (see Methods). Specifically, we calculated and classified the fixed points of mean-field equations for different values of σ_e and σ_i for the values of drives studied in the spiking networks. The fixed point(s) of the mean-field (for the excitatory population, U_e) are plotted in the second row of each panel in Figure 4. These values correspond to population averages of the (unitless) membrane potential analogue taken across the individual units in our spiking networks (u_j). We then performed linear stability analysis for those fixed points. By doing so, we extracted eigenvalues which determine the fixed points' stability, and how it might change as input drive is varied. The dampening rate represents the speed at which the system is either repelled from or returns to its fixed point(s) and thus classifies their stability (i.e., the real components of eigenvalues associated with each fixed point). The dampening rate is plotted in the row below the fixed points, followed by the frequency of oscillatory fixed points (i.e., the imaginary components of eigenvalues associated with each fixed point).

These mean-field analyses confirm that both excitatory and inhibitory heterogeneity have notable impacts on changes in network dynamics analogous to seizure-onset. In the top row of each panel in Figure 4 we present quantifications of our spiking network dynamics as in Figure 3, but averaged over 100 independent simulations. In the presence of high heterogeneity (whenever σ_e and/or σ_i are large, i.e., Figure 4**(a)**, **(b)**, and **(d)**), increased drive results in a smooth and approximately linear increase in both mean activity and synchrony. The mean-field analyses of the associated systems reveal a single fixed point, whose value increases monotonically with drive. Oscillation frequency is low, indicative of slow-wave activity. In Figure 4**(d)** (low σ_e, high σ_i) synchrony emerges through a supercritical Hopf bifurcation (35) at a high level of drive (the stable fixed point becomes unstable, giving rise to a stable limit cycle). The reverse bifurcation is observed in Figure 4**(a)** (the unstable fixed point becomes stable) while the behavior of the spiking network exhibits gradual change in synchrony: this is due to the noise in the spiking networks which allows for the presence of quasi-cycles (36).

In contrast to these cases, spiking networks with low heterogeneity (low σ_e and σ_i, Figure 4**(c)**) exhibit sudden increases in mean activity and synchrony. The associated mean-field system displays multistability: it possesses multiple fixed points. As the input drive increases, two of these fixed points coalesce and disappear via a saddle-node bifurcation (35). The system's mean activity is thus suddenly drawn towards a preexisting large-amplitude limit cycle. This transition occurs at a drive corresponding with the sudden increase in synchrony and mean activity seen in the spiking network. In the mean-field system, the frequency of resulting oscillations are found to be faster compared to the high heterogeneity scenarios, further emphasizing the uniqueness of the properties of the dynamical system with low heterogeneity.

We note that the more notable inter-trial variability in Figure 4**(d)** (as illustrated by the fainter $\pm$ SD curves) results from the variable (yet gradual) onset of increased synchrony, in contrast to the transition in Figure 4**(c)** which occurs at a specific drive. The different timings of the onset of synchrony in each independent simulation yield oscillations at different relative phases, which explains why oscillations are not observed in our averaged firing rate measures displayed in Figure 4 (notably, such oscillations are subtle even in the single simulation visualizations of Figure 3 given the 100 ms sliding time window); rather, the presence of oscillatory activity is demarcated by a notable increase in the mean Synchrony Measure.

To facilitate the comparison of our spiking networks with our mean-field calculations, we developed a Bifurcation Measure (see Methods) quantifying the tendency for sudden changes in the activity of the spiking network. Higher values of this measure indicate the presence of a sudden transition in the relationship between the quantification of interest and the drive. Given the more subtle qualitative difference in the

DRAFT

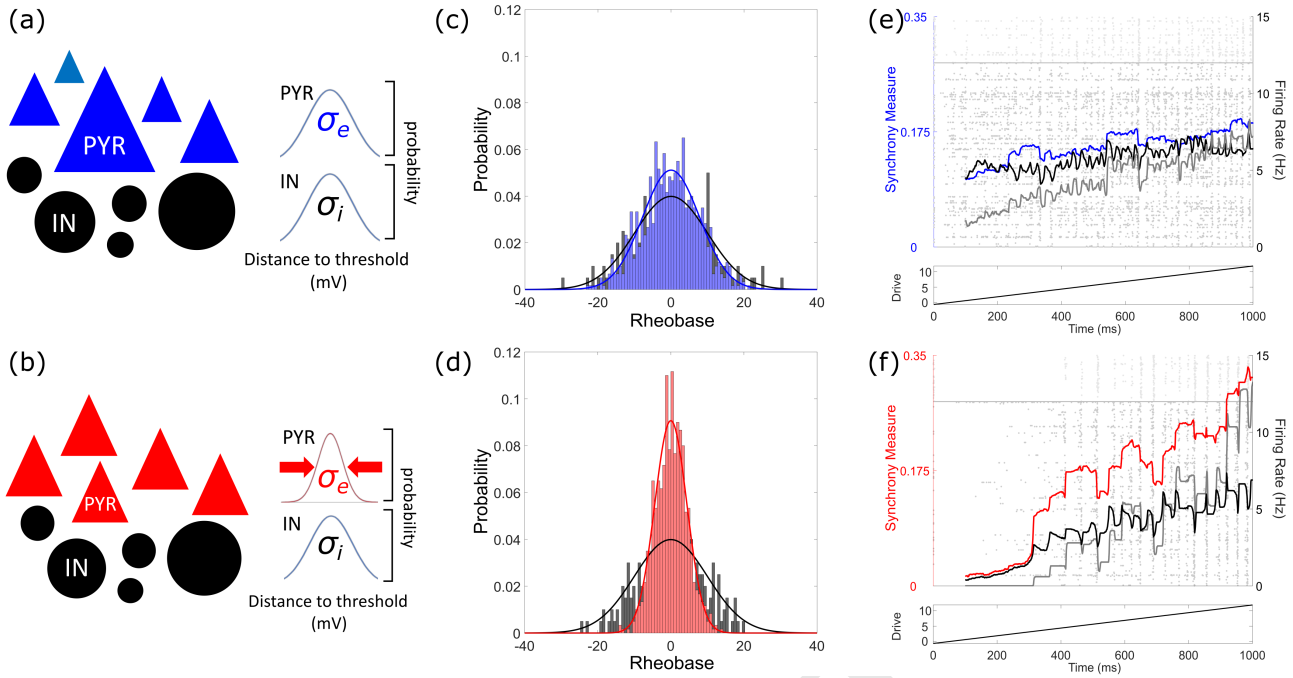

Fig. 2. Experimentally observed decreases in heterogeneity amongst excitatory cells promote ictogenic-like transitions in E-I spiking neural network models. **(a-b)**: Schematic representation of model spiking E-I networks, with pyramidal neurons represented as triangles and interneurons as circles. Blue neurons represent non-epileptogenic (i.e. high) levels of heterogeneity (see also the variable neuron sizes) while red neurons represent epileptogenic (i.e. low) levels of heterogeneity (see also the similar neuron sizes). This color schema is maintained in the remaining figures. Here, the inhibitory (black neurons) heterogeneity is set at a moderate value amongst the range studied ($\sigma_i = 10.0$ mV), while $\sigma_e = 7.8$ mV in panel **(a)** and $\sigma_e = 4.4$ mV in panel **(b)**. **(c-d)**: Visualizations of the distribution of model rheobases, with the solid curve (red or blue for excitatory neurons, black for inhibitory neurons) illustrating the Gaussian function and the corresponding histogram illustrating the example random distribution underlying the simulations in this figure. **(e-f)**: Example simulations with a linearly increasing excitatory drive. Background: raster plot of network activity, with each circle representing the firing of an action potential of the associated neuron (excitatory neurons below horizontal line, inhibitory neurons above). Foreground: quantifications of network activity taken over 100 ms sliding time windows, with the excitatory synchrony quantified by the Synchrony Measure in blue or red (left axis) depending on the excitatory heterogeneity level, as well as excitatory (black) and inhibitory (grey) population firing rates (right axis) Bottom: drive ($I(t)$) to the excitatory population.

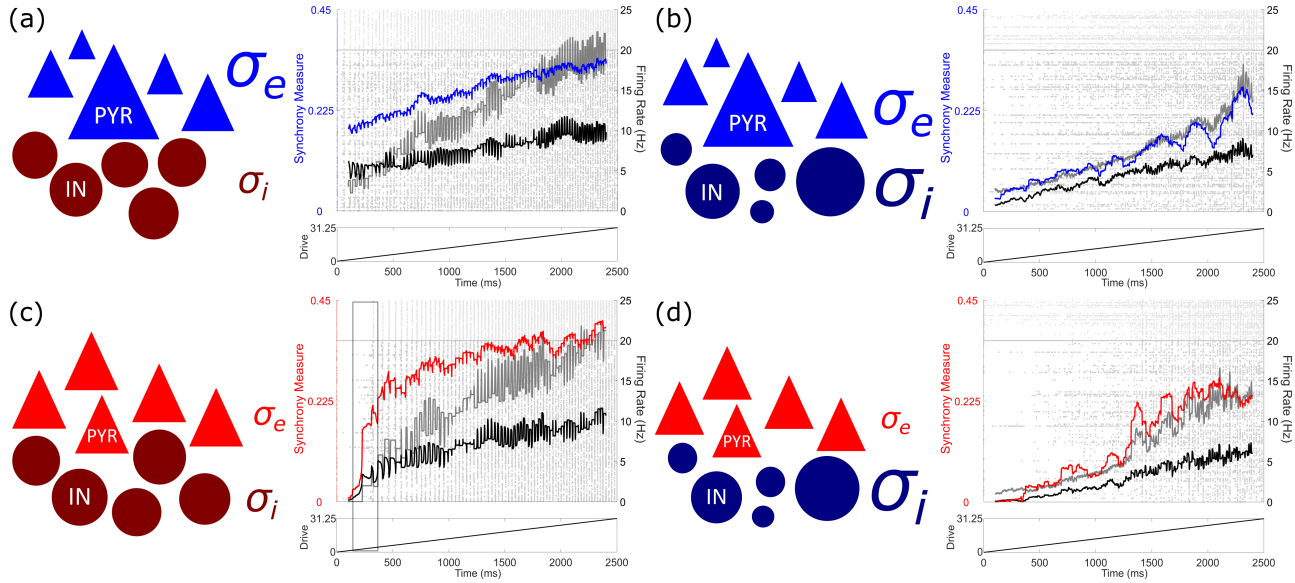

Fig. 3. Effects of varied inhibitory heterogeneity on sudden transitions into synchrony in E-I spiking neural network models. Schematics and single simulation visualizations following the conventions of Figure 2 (with inhibitory heterogeneity reflected by darker shaded blue and red neurons), now shown for four combinations of excitatory and inhibitory heterogeneities: $\sigma_e = 7.8$ mV and $\sigma_i = 2.5$ mV in panel **(a)**, $\sigma_e = 7.8$ mV and $\sigma_i = 16.75$ mV in panel **(b)**, $\sigma_e = 4.4$ mV and $\sigma_i = 2.5$ mV in panel **(c)**, and $\sigma_e = 4.4$ mV and $\sigma_i = 16.75$ mV in panel **(d)**. Relative sizes of σ_e and σ_i represent the relative heterogeneity levels. Sudden transitions into high levels of excitatory synchrony are seen in panel **(c)** and **(d)**, with the transition in panel **(c)** yielding a notably higher level of synchrony (highlighted by the grey box). Meanwhile, changes in the dynamics of panels **(a)** and **(b)** are largely linear, with the excitatory synchrony consistently lower when both excitatory and inhibitory heterogeneities are at their highest in panel **(b)**.

firing rates in our spiking networks, we applied the Bifurcation Measure to the excitatory firing rate (B_e) for the four combinations of σ_e and σ_i examined in Figure 4. This revealed more sudden changes with low σ_e and σ_i (B_e=0.1050) as opposed to any other scenario (high σ_e, low σ_i, B_e=0.0416; high σ_e, high σ_i, B_e=0.0148; low σ_e, high σ_i, B_e=0.0333) where the transition is smoother. This analysis indicates that the dynamical transition present in Figure 4**(c)** is not only unique in the magnitude of the synchronous onset, but also in an associated sudden increase in firing rates.

Since the seizure state is typified both by increased synchrony and firing rates (2, 14), this analysis confirms that the sharp transition in these quantities only observed in spiking models with low heterogeneity is driven by a saddle-node bifurcation (Figure 4**(c)**). These results echo other seizure modeling studies showcasing that ictogenic transitions can arise driven by mathematical bifurcations, and specifically the observation that saddle-node bifurcations underlie abrupt seizure-onset dynamics (4, 5, 28). As a corollary, high heterogeneity improves network resilience to sudden changes in synchrony by preventing multistability and fostering gradual changes in network firing rate and oscillatory behavior.

Asymmetric effects of excitatory and inhibitory heterogeneity. Figure 4 highlights distinct effects of excitatory versus inhibitory heterogeneity on the onset of synchrony in spiking networks and the structure of mean-field systems (see the differences between Figure 4**(a)** and **(c)**). To clarify these effects we explored a larger parameter space of σ_e and σ_i, as shown in Supplementary Figure S2. For each heterogeneity combination we applied the Bifurcation Measure to excitatory synchrony (B, hereafter referred to simply as the Bifurcation Measure; see details in Methods), which quantifies the presence of sudden changes in network synchrony in response to a changing network drive. This exploration confirms the asymmetric effect of excitatory and inhibitory heterogeneity on these sudden transitions, with a moderate value of B for low σ_e and high σ_i but a minimal value of B for high σ_e and low σ_i, comporting with patterns observed in previous computational literature (37).

Similar asymmetry is seen in our spiking network dynamics (B in Supplementary Figure S2**(a)** and the Synchrony Measure S in Supplementary Figure S2**(b)**) and our mean-field systems (the bolded regime of networks exhibiting multi-stability in Supplementary Figure S2**(a)** and the bolded regime of networks exhibiting an unstable fixed point in Supplementary Figure S2**(b)**). We show an example visualization of the fixed points and their classifications in Supplementary Figure S3. In Supplementary Figure S4 we show the pattern followed by B is robust to changes in connectivity density. Supplementary Figure S5 shows the details of the determination of fixed point stability in Supplementary Figure S2**(b)**. We further used the Bifurcation Measure to see whether the asymmetric effects of excitatory and inhibitory heterogeneity are generalizable. In the four exemplar cases highlighted in Figures 3 and 4 this is the case for reasonable changes to any of our synaptic strengths, as shown in Supplementary Figure S6. The generalizability of our mathematical analyses can be inferred from analyses performed on a similar network in previous work (see the Supplementary Material of Rich et. al. (34)).

This analysis shows that notable decreases in B occur at higher values of σ_i than they do for σ_e, a result which has important implications for our understanding of the potentially differing roles of excitatory and inhibitory heterogeneity in seizure resilience (see Discussion).

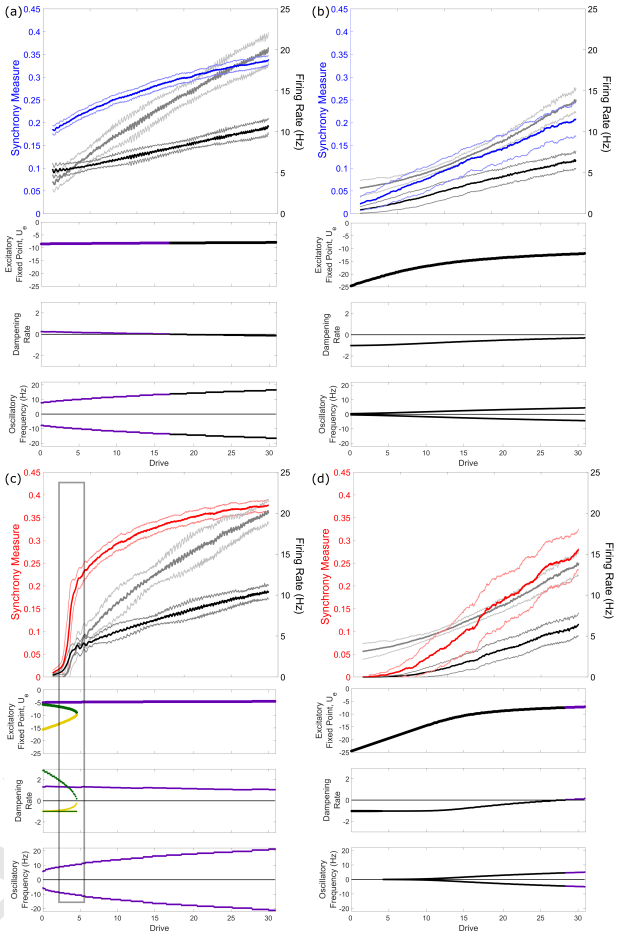

Fig. 4. Effects of heterogeneity on spiking network dynamics is explained by stability analysis of mean-field equations. Panels correspond to heterogeneity levels studied in Figure 3. Top row: measures of spiking network dynamics (as seen in Figures 2 and 3) averaged over 100 simulations (dark curve=mean, lighter curve=± one SD). Remaining rows: results of stability analysis on mean-field equations corresponding with these networks visualized via the fixed point of mean excitatory activity (top), and the dampening rate (i.e., the real components of the eigenvalues, middle) and oscillatory frequency (i.e., the imaginary components of the eigenvalues, bottom) associated with each fixed point. Green and gold coloring are used to differentiate the three distinct fixed points in panel c, while the stability of fixed points is color coded (purple=unstable, i.e., positive dampening rate; black=stable, i.e., negative dampening rate. Notably, only in panel **(c)**, where both heterogeneity levels are low, do we see multiple fixed points and a saddle-node bifurcation that occurs at a value of the drive corresponding with the sudden transition in spiking networks (highlighted by the grey box).

Differences in population averaged activation functions explained by differences in neural heterogeneity. Finally, we return to the counter-intuitive differences in activation functions measured experimentally. As noted previously, the population of neurons from epileptogenic tissue exhibited qualitatively and quantitatively different activation functions via non-linear and hypo-active firing responses (Figure 1**(c)**).

To understand if heterogeneity accounts for these observations, we computed analytically the averaged activation functions of the excitatory populations in our model networks. In Figure 5**(a)**, the experimentally derived firing frequencies

from epileptogenic frontal lobe and non-epileptogenic MTG are plotted alongside activation functions of our model populations. For low heterogeneity, the model population's activation function captured both the non-linear and low firing rate responses measured experimentally for neurons in the epileptogenic zone. The increased excitability and linearity seen experimentally in non-epileptogenic tissue was captured by the averaged activation function for our more heterogeneous model population. This comparison is appropriate considering the FI curve data from Figure 1**(c)** is averaged over the populations of interest, and is thus analogous to the population activation function of our model neurons.

To quantitatively support this correspondence, we found the values of σ_e that best fit our experimental data using a non-linear least squares method (see details in Methods). The data from epileptogenic frontal lobe was best fit by an activation function (see Equation 12) with $\sigma_e = 5.0$ mV (r^2=0.94), while the data from non-epileptogenic MTG was best fit by an activation function with $\sigma_e = 7.8$ mV (r^2=0.98). That the best-fit values closely match the experimentally-observed heterogeneity values means the features of our epileptogenic (resp. non-epileptogenic) activation curves are captured by neural populations with low (resp. high) heterogeneity.

This somewhat counter-intuitive result is explained by the linearizing effect that increased heterogeneity, and noise more generally, has on input-output response functions (37, 38). This effect is illustrated in Figure 5**(b)**. The bolded sigmoids represent the averaged activity of the entire population of heterogeneous neurons alongside individual activation functions (fainter sigmoids). Increased (resp. decreased) variability dampens (resp. sharpens) the averaged response curve for the non-epileptogenic (resp. epileptogenic) setting. Such variability-induced linearization raises the excitability at low input values, corresponding with the dynamics highlighted in Figure 5**(a)**. Figure 5 illustrates that our model predicts significant differences in the activation function between epileptogenic and non-epileptogenic tissue, and that heterogeneity, or lack thereof, can explain counter-intuitive neuronal responses. However, these differences are not necessarily reflected in network dynamics, as illustrated by the similar network firing rates in Figure 4**(a)** and **(c)** at high levels of drive. In the context of seizure, this implies that excessive synchronization of a neural population need *not* be exclusively associated with increased excitability as represented by a lower firing threshold or higher firing rate of the population of isolated neurons.

Discussion

In this work, we propose that neural heterogeneity serves an important role in generating resilience to epileptogenesis, and correspondingly that its loss may be a "final common pathway" for a number of etiologies associated with epilepsy. We explored this hypothesis using *in vitro* electrophysiological characterization of human cortical tissue from epileptogenic and non-epileptogenic areas, which revealed significant differences in DTT (a key determinant of neuronal excitability) heterogeneity in the pathological and non-pathological settings. The ability to perform experiments on tissue from human subjects diagnosed with epilepsy makes these results particularly relevant to the human condition. We then implemented these experimentally observed heterogeneities in an analogous parameter in *in silico* spiking neural networks. Our explorations show that networks with high heterogeneity, similar to the physiological setting, exhibit a more stable asynchronously firing state that is resilient to sudden transitions into a more active and synchronous state. Differing heterogeneity levels also explained the significant differences in the experimentally-obtained population activation functions between epileptogenic and non-epileptogenic tissue. Finally, using mathematical analysis we show that differences in the bifurcation structure of analogous mean-field systems provide a theoretical explanation for dynamical differences in spiking networks. Viewed jointly, these three avenues of investigation provide strong evidence that reduction in biophysical heterogeneity *exists* in epileptogenic tissue, can *yield dynamical changes* with parallels to seizure onset, and that there are *theoretical principles* underlying these differences.

Computational studies have established the role played by heterogeneity in reducing synchronous activity in the context of physiological gamma rhythms (39–41). Other computational investigations have implemented heterogeneity in more varied neural parameters (42) and identified asymmetric effects of excitatory and inhibitory heterogeneities on network dynamics (37, 43). Our study complements and extends the understanding of the role of biophysical heterogeneity in neural networks to human epilepsy by: 1) using experimentally derived heterogeneities of the DTT in non-epileptogenic and epileptogenic surgical specimens, which when implemented *in silico* are dynamically relevant; 2) exploring the effects of heterogeneity on the transition to synchrony, the hallmark of seizure onset; 3) detailing the differing extents to which inhibitory and excitatory heterogeneity contribute to circuit resilience to synchronous transitions. Our mathematical analysis further builds on this work to provide a theoretical undergird for these observed dynamics.

The asymmetric effect of excitatory and inhibitory heterogeneities is interesting, and supports predictions regarding inhibitory heterogeneity's role in ictogenesis. Supplementary Figure S2**(a)** shows that the sudden onset of synchrony is more likely to arise for moderate values of σ_i than σ_e. The physiological heterogeneity of the entire inhibitory population is likely to be larger than for the excitatory population (44), driven in part by the diverse subpopulations of interneurons (45). Thus, our work makes two interesting predictions: first, a moderate loss of heterogeneity amongst inhibitory interneurons might be sufficient to make a system vulnerable to ictogenesis; second, the preservation of inhibitory heterogeneity may provide a bulwark against ictogenesis even if excitatory heterogeneity is pathologically reduced as observed experimentally. Of note is that, in this work, changes in heterogeneity are "symmetric" (i.e., increased heterogeneity results in a similar increase in both hyper- and hypo-active neurons). A subject of future investigation is whether increasing the heterogeneity of the system "asymmetrically" (i.e., by only adding hyper or hypo-active neurons to the population) would yield similar effects.

The loss of inhibitory cell types (16, 17) or unique firing patterns of inhibitory cells (46) previously shown to be associated with epilepsy can be thought of as a loss of inhibitory heterogeneity. These studies tend to contextualize the epileptogenic effect of these changes as driven by a deficit in GABAergic signalling, either due to the loss of inhibitory cells (17) (or, in the case of (16), the loss of specifically dendritic targeting

DRAFT

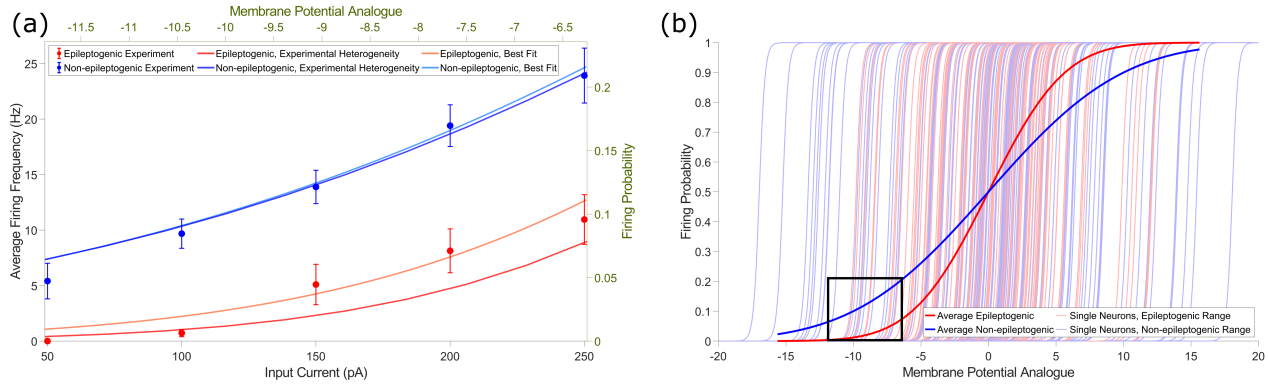

Fig. 5. Differing levels of neural heterogeneity explain population activation function differences observed experimentally between epileptogenic and non-epileptogenic cortex. **(a)**: Experimentally observed firing frequencies plotted against input current (left and bottom axes, mean $\pm$ SEM) for epileptogenic frontal lobe (red) and non-epileptogenic MTG (blue) tissue (as shown previously in Figure 1**(c)**), visualized against an analogous measure of the relationship between population activity (firing probability) and drive (membrane potential analogue) in our neuron models (right and top axes, details in Methods). The shape of the curve for the heterogeneity value derived from epileptogenic tissue experimentally (red, $\sigma_e = 4.4$) qualitatively matches the experimental data, and a best fit (light red, $\sigma_e = 5.03$, r^2=0.94) is obtained with a similarly low heterogeneity value. In contrast, the curve associated with the heterogeneity value derived from non-epileptogenic tissue experimentally (blue, $\sigma_e = 7.8$) closely matches the experimental data from non-epileptogenic tissue and is nearly identical to the best fit (light blue, $\sigma_e = 7.77$, r^2=.98). **(b)**: A visualization of the entirety of the sigmoidal input-output relationship for our neuron models, with the regime compared to experimental data in panel **(a)** in a black box. Fainter curves represent input-output relationships for individual neurons, either epileptogenic (red) or non-epileptogenic (blue): the wider variability in the blue curves yields the flatter sigmoid representing the population activation function for our non-epileptogenic heterogeneity value, and vice-versa for the red curves associated with the epileptogenic heterogeneity value.

inhibitory signaling) or to fewer action potentials generated by inhibitory cells (46). We present a potential additional route to the seizure state under such conditions, where the loss of inhibitory neuronal heterogeneity promotes ictogenesis, which could serve to reconcile these studies' sometimes conflicting observations regarding the loss of interneurons.

How might the decreased cellular and population excitability through homogenization of neuronal excitability we observed be reconciled with the perspective of epilepsy as a disorder of hyper-excitability? Our findings suggest that within the epileptogenic zone, interictal hypometabolism (47) and manifestations of "hyper-excitability," such as inter-ictally recorded high-frequency oscillations (HFOs) and inter-ictal spikes (IIDs) (48, 49), indeed can coexist. In essence, our findings suggest that the observed hypometabolism may arise in part from cellular homogenization that reduces overall population excitability (see Figure 1**(c)** and 5**(b)**) - since metabolism is tightly linked to maintaining ionic gradients and thus firing rates - while simultaneously facilitating the emergence of synchronous activities (Figure 4**(c)**) such as HFOs, IIDs and seizures. In addition, our work also hints at a process of "disinhibition through neural homogenization" - decreased population excitability in inhibitory populations through homogenization, together with our observation that sudden transitions occurred for more moderate values of σ_i, indicates suppression in overall inhibition. Such disinhibition may further explain the hypometabolism observed interictally given that interneuronal spiking appears to contribute more to brain metabolism than pyramidal cells (50). While conjectural, further studies using targeted patching of interneurons in both human and chronic rodent models are warranted to answer these questions, and characterize what, if any, homogenization occurs in interneuronal populations during epileptogenesis and epilepsy.

While our results include lower neuronal counts from the frontal lobe, this represents a less common source of human cortical tissue than non-epileptogenic MTG. Although one might obtain a greater sample by comparing non-epileptogenic MTG to epileptogenic mesial temporal structures (i.e., subiculum, parahippocampal gyrus, hippocampus) this would represent comparison between the allocortex and neocortex which would add a further confound. Alternatively, obtaining non-epileptogenic medial temporal lobe (MTL) cortex is exceedingly rare. With these important limitations in the access to human cortical tissue considered, our comparison between epileptogenic frontal lobe, non-epileptogenic (tumor) frontal lobe, and non-epileptogenic MTG represent a best-case comparison of the biophysical properties of epileptogenic and non-epileptogenic human tissue while reasonably controlling for confounds introduced by the differing brain regions.

Our model networks, while analogous to E-I microcircuits commonly used in computational investigations of cortical activity (8, 29, 30), are simplified from the biophysical reality and must be considered with these limitations in mind; indeed, such models cannot reasonably capture the full richness and complexity of seizure dynamics and do not include multiple inhibitory populations (45). However, this simplifying choice facilitates findings that have their foundation in fundamental mathematical principles and are not especially reliant on biophysical intricacies such as network topology (see the Supplementary Material of (34)). This increases the likelihood that these predictions are generalizable. Potential future work involves the use of more biophysically detailed human inspired neuron and network models, allowing for the implementation and study of additional types of heterogeneity (including multiple, diverse inhibitory populations) and/or the study of model seizures. Such studies will be facilitated by our recent development of a biophysically-detailed computational model of a human L5 cortical pyramidal neuron (51), allowing them to be more directly applicable to potential clinical applications for the treatment of human epilepsy. In this vein, while we do not model seizures per se in this work, the two most common types of seizure onsets observed in intracranial recordings are the low-voltage fast (52) and hyper-synchronous onsets (53). Both reflect a sudden transition from a desynchronized state to a

DRAFT

synchronous oscillation, albeit of differing frequencies. Given the ubiquity of such onsets, our modelling of the transition to synchrony is likely to be broadly relevant to epilepsy.

Lastly, one might wonder what neurobiological processes render an epileptogenic neuronal population less biophysically diverse. While under physiological conditions channel densities are regulated within neurons to obtain target electrical behaviors (54), it remains speculative as to what processes might lead to pathological homogenization of neuronal populations. However, modeling suggests that biological diversity may be a function of input diversity, and thus "homogenizing the input received by a population of neurons should lead the population to be less diverse" (13). Although requiring further exploration, it is possible that the information-poor, synchronous post-synaptic barrages accompanying seizure (15) represent such a homogenized input, reducing a circuit's resilience to synchronous transitions and promoting epileptogenesis by reducing biophysical heterogeneity.

Materials and Methods

Experiment: Human brain slice preparation. All procedures on human tissue were performed in accordance with the Declaration of Helsinki and approved by the University Health Network Research Ethics board. Patients underwent a standardized temporal or frontal lobectomy (55) under general anesthesia using volatile anesthetics for seizure treatment (56). Tissue was obtained from patients diagnosed with temporal or frontal lobe epilepsy who provided written consent. Tissue from temporal lobe was obtained from 22 patients, age ranging between 21 to 63 years (mean age ± SEM: 37.8 ± 2.9). The resected temporal lobe tissue displayed no structural or functional abnormalities in preoperative MRI and was deemed "healthy" tissue considering it is located outside of the epileptogenic zone. Tissue from frontal lobe was obtained from five patients, age ranging between 23-36 years (mean age ± SEM: 30.2 ± 2.4), and was deemed "epileptogenic" tissue as it was obtained from the epileptogenic zone. Tissue from non-epileptogenic frontal lobe obtained during tumor resection was obtained from two patients, age ranging between 37-58 years (mean age ± SEM: 47.5 ± 10.5), and was also considered "non-epileptogenic".

After surgical resection, the cortical tissue block was instantaneously submerged in ice-cold (∼4°C) cutting solution that was continuously bubbled with 95% O_2-5% CO_2 containing (in mM): sucrose 248, KCl 2, $MgSO_4.7H_2O$ 3, $CaCl_2.2H_2O$ 1, $NaHCO_3$ 26, $NaH_2PO_4.H_2O$ 1.25, and D-glucose 10. The osmolarity was adjusted to 300-305 mOsm. The human tissue samples were transported (5-10 min) from Toronto Western Hospital (TWH) to the laboratory for further slice processing. Transverse brain slices (400 μm) were obtained using a vibratome (Leica 1200 V) perpendicular to the pial surface to ensure that pyramidal cell dendrites were minimally truncated (56, 57) in the same cutting solution as used for transport. The total duration, including slicing and transportation, was kept to a maximum of 20-30 minutes. After sectioning, the slices were incubated for 30 min at 34°C in standard artificial cerebrospinal fluid (aCSF) (in mM): NaCl 123, KCl 4, $CaCl_2.2H_2O$ 1, $MgSO_4.7H_2O$ 1, $NaHCO_3$ 26, $NaH_2PO_4.H_2O$ 1.2, and D-glucose 10. The pH was 7.40 and after incubation the slice was held for at least for 60 min at room temperature. aCSF in both incubation and recording chambers were continuously bubbled with carbogen gas (95% O_2-5% CO_2) and had an osmolarity of 300-305 mOsm.

Experiment: Electrophysiological recordings and intrinsic physiology feature analysis. Slices were transferred to a recording chamber mounted on a fixed-stage upright microscope (Axioskop 2 FS MOT; Carl Zeiss, Germany). Recordings were performed from the soma of pyramidal neurons at 32-34° in recording aCSF continually perfused at 4 ml/min. Cortical neurons were visualized using an IR-CCD camera (IR-1000, MTI, USA) with a 40x water immersion objective lens. Using the IR-DIC microscope, the boundary between layer 1 (L1) and 2 (L2) was easily distinguishable in terms of cell density. Below L2, the sparser area of neurons (L3) was followed by a tight band of densely packed layer 4 (L4) neurons, with a decrease in cell density indicating layer 5 (L5) (22, 25).

Patch pipettes (3-6 MΩ resistance) were pulled from standard borosilicate glass pipettes (thin-wall borosilicate tubes with filaments, World Precision Instruments, Sarasota, FL, USA) using a vertical puller (PC-10, Narishige). Pipettes were filled with intracellular solution containing (in mM): K-gluconate 135; NaCl 10; HEPES 10; $MgCl_2$ 1; Na_2ATP 2; GTP 0.3, pH adjusted with KOH to 7.4 (290–309 mOsm). In a subset of experiments the pipette solution also contained biocytin (3-5%).

Whole-cell patch-clamp recordings were obtained using a Multiclamp 700A amplifier, Axopatch 200B amplifier, pClamp 9.2 and pClamp 10.6 data acquisition software (Axon instruments, Molecular Devices, USA). Electrical signals were digitized at 20 kHz using a 1320X digitizer. The access resistance was monitored throughout the recording (typically between 8-25 MΩ), and neurons were discarded if the access resistance was >25 MΩ. The liquid junction potential was calculated to be -10.8 mV and was not corrected.

Electrophysiological data were analyzed off-line using Clampfit 10.7, Python and MATLAB (58). Electrophysiological features were calculated from responses elicited by 600 ms square current steps as previously described (22). Briefly, the resting membrane potential (RMP) was measured after breaking into the cell (IC=0). The firing threshold was determined following depolarizing current injections between 50 to 250 pA with 50 pA step size for 600 ms; the threshold was calculated by finding the voltage value corresponding with a value of $\frac{dV}{dt}$ that was 5% of the average maximal $\frac{dV}{dt}$ across all action potentials elicited by the input current that first yielded action potential firing. The distance to threshold presented in this paper was calculated as the difference between the RMP and threshold. The average FI curve (i.e., activation function) was generated by calculating the instantaneous frequency at each spike for each of the depolarizing current injections (50-250 pA, step size 50 pA, 600 ms) and averaging over the population. Spike frequency adaptation ratio was calculated using the "hero" sweep (defined as the sweep between 39 to 61 pA greater than the rheobase). The adaptation ratio was defined as the mean of the last 2 interspike intervals divided by the mean of the first two interspike intervals.

Plotting of experimental data was performed using GraphPad Prism 6 (GraphPad software, Inc, CA, USA). The non-parametric Mann-Whitney test was used to determine statistical differences between the means of two groups. The F-test was used to compare standard deviation (SD) between groups. The two sample coefficient of variation test was used to compare the coefficient of variance (CV) between groups. Normality of the data was tested with the Shapiro-Wilk and D'Agostino & Pearson omnibus normality tests with alpha=0.05. The one-way ANOVA post hoc with Dunn's multiple comparison test was used to determine statistical significance in the adaptation ratio. A standard threshold of $p<0.05$ is used to report statistically significant differences.

Modeling: spiking neural network. The cortical spiking neural network contains populations of recurrently connected excitatory and inhibitory neurons (59, 60). The spiking response of those neurons obeys the non-homogeneous Poisson process

$$Y_j \rightarrow Poisson(f(u_j, h_j)) \quad [1]$$

where $Y_j = \sum_l \delta(t - t_k)$ is a Poisson spike train with rate $f(u_j, h_j)$.

The firing rate of neuron j is determined by the non-linear sigmoidal activation function $f(u_j, h_j)$,

$$f(u_j, h_j) = \frac{1}{1 + e^{-\beta(u_j - h_j)}} \quad [2]$$

where u_j is the membrane potential analogue and h_j represents the rheobase. The constant $\beta = 4.8$ scales the non-linear gain.

Heterogeneity is implemented via the rheobases h_j. The h_j values are chosen by independently and randomly sampling a normal Gaussian distribution whose standard deviation is $\sigma_{e,i}$ if neuron j is excitatory (e) or inhibitory (i). The values of σ_i and σ_e are varied throughout these explorations between a minimum value of 2.5 mV and a maximum value of 16.75 mV. The heterogeneity parameters for the model have a direct parallel with the heterogeneity in the

DRAFT

distance to threshold (DTT) measured experimentally, with β chosen so that the experimentally observed heterogeneity values and the heterogeneity parameters implemented in the model are within the same range (compare Figure 1**(b)** and Figure 2**(c-d)**).

The membrane potential analogue u_j is defined by

$$\frac{du_j}{dt} = \alpha_x \left(-u_j(t) + Syn_j^{ex} + Syn_j^{ix} + I_x + I(t)\right) + \sqrt{2\alpha_x D} X_j \quad [3]$$

The variable α_x represents the time constant depending upon whether the neuron j is excitatory ($x = e, \alpha_e = 10$ ms) or inhibitory ($x = i, \alpha_i = 5$ ms). The differential time scales are implemented given the different membrane time constants between cortical pyramidal neurons and parvalbumin positive (PV) interneurons (33).

Syn_j^{ex} and Syn_j^{ix} are the synaptic inputs to the cell j (from the excitatory and inhibitory populations, respectively), dependent upon whether cell j is excitatory ($x = e$) or inhibitory ($x = i$). Our cortical model is built of 800 excitatory and 200 inhibitory neurons (61–63). The connectivity density for each connection type (E-E, E-I, I-E, and I-I) is varied uniformly via a parameter p. In this study, $p = 1$ is used (i.e., all-to-all connectivity) with the exception of in Supplementary Figure S4. The synaptic strengths are represented by w_{xy} where $x, y = e, i$ depending upon whether the pre-synaptic cell (x) and the post-synaptic cell (y) are excitatory or inhibitory. In our model, $w_{ee} = 100.000$, $w_{ei} = 187.500$, $w_{ie} = -293.750$, and $w_{ii} = -8.125$. Negative signs represent inhibitory signalling, while positive signs represent excitatory signalling. These values are chosen to place the network near a tipping point between asynchronous and synchronous firing based on mathematical analysis and previous modeling work (34), and scaled relative to the values of β.

The post-synaptic inputs Syn_j^{ex} and Syn_j^{ix} are given by

$$Syn_j^{ex} = \frac{1}{800} \sum_{k=1, k\neq j}^{800} c_{kj} \frac{w_{ex}}{p} Y_k(t - \Delta t) \quad [4]$$

$$Syn_j^{ix} = \frac{1}{200} \sum_{k=1, k\neq j}^{200} c_{kj} \frac{w_{ix}}{p} Y_k(t - \Delta t) \quad [5]$$

where $x = e, i$ and Y_k is a Poisson spike train given by $Y_k = \sum_l \delta(t - t_l)$. The connectivity scheme excludes auto-synapses. c_{kj} represents the connectivity: if neuron k synapses onto neuron j, $c_{kj} = 1$, and otherwise $c_{kj} = 0$. The synaptic weights are scaled by the connectivity density p so that the net input signal to each neuron is not affected by the number of connections.

Equation 3 includes three non-synaptic inputs to the neuron: I_x, $I(t)$, and and $\sqrt{2\alpha_x D} X_j$. The variable X_j is a spatially independent Gaussian white noise process. The value of noise intensity was chosen so that the noise-induced fluctuations are commensurate with endogenous dynamics of the network. I_x represents a bias current whose value depends on whether the neuron is excitatory ($x = e$) or inhibitory ($x = i$), imparting a differential baseline spiking rate to these distinct populations. Here, $I_i = -31.250$, ensuring that inhibitory neurons will typically require excitatory input to fire, matching biophysical intuition. $I_e = -15.625$ is based on previous literature (31–34) to position the system near the transition between asynchronous and synchronous firing.

$I(t)$ implements time-varying external input only applied to the excitatory population (this is simply referred to as the "drive" to the system in Figures 2, 3 and 4). In this work, this term is used primarily to study the response of the spiking network to a linear ramp excitatory input that occurs at a time scale much slower than the dynamics of individual neurons: to yield the ramp current used throughout the study $I(t)$ simply varies linearly between 0 and 31.25 over a 2500 ms simulation (for computational efficiency, the simulation length is limited to 2048 ms for the heatmaps displayed in Supplementary Figures S2 and S4). In Supplementary Figure S2**(b)**, where we characterize the dynamics of the network with constant input, $I(t) = 15.625$ uniformly.

The final probability of a Poisson neuron j firing at time t depends upon the effect of these various elements on u_j:

$$\rho_j = 1 - e^{-f(u_j(t), h_j)dt} \quad [6]$$

Parameter values. Parameter values summarized in Table 1 below are analogous to those used in previous work on oscillatory cortical networks (31–34) with the scaling of our chosen β accounted for.

Table 1. Key model parameters.

Parameter	Value
Number of excitatory neurons	800
Number of inhibitory neurons	200
Excitatory time constant, α_e	10 ms
Inhibitory time constant, α_i	5 ms
Non-linear gain of activation function, β	4.8
Variance of noisy input, D	3.906
Excitatory bias current, I_e	-15.625
Inhibitory bias current, I_i	-31.250
External input, $I(t)$	Variable
Excitatory-excitatory synaptic strength, w_{ee}	100.000
Excitatory-inhibitory synaptic strength, w_{ei}	187.500
Inhibitory-inhibitory synaptic strength, w_{ii}	-8.125
Inhibitory-excitatory synaptic strength, w_{ie}	-293.750
Excitatory heterogeneity, σ_e	Variable
Inhibitory heterogeneity, σ_i	Variable
rheobase, h	Variable
Connectivity density, p	Variable
Time step, Δt	1 ms

Numerics. All sampling from standard normal Gaussian distributions is done via the Box-Mueller algorithm (64). Equations are integrated using the Euler-Maruyama method. In our simulations, $\Delta t = 0.1$, scaled so that each time step Δt represents 1 ms.

The excitatory network synchrony (i.e. Synchrony Measure) and excitatory and inhibitory firing rates are calculated over sliding 100 ms time windows in Figures 2, 3 and 4. To preserve symmetry and ensure initial transients do not skew the data, our first window begins at $t = 100$.

The Synchrony Measure is an adaptation of a commonly used measure developed by Golomb and Rinzel (65, 66) to quantify the degree of coincident spiking in a network as utilized in our previous studies (62, 63, 67, 68). Briefly, the measure involves convolving a very narrow Gaussian function with the time of each action potential for every cell to generate functions $V_i(t)$. The population averaged voltage $V(t)$ is then defined as $V(t) = \frac{1}{N} \sum_{i=1}^{N} V_i(t)$, where N is the number of cells in the network. The overall variance of the population averaged voltage $\mathrm{Var}(V)$ and the variance of an individual neuron's voltage $\mathrm{Var}(V_i)$ is defined as

$$\mathrm{Var}(V) = < V(t)^2 > - < V(t) >^2 \quad [7]$$

and

$$\mathrm{Var}(V_i) = < V_i(t)^2 > - < V_i(t) >^2 \quad [8]$$

where $< \cdot >$ indicates time averaging over the interval for which the measure is taken. The Synchrony Measure S is then defined as

$$S = \frac{\mathrm{Var}(V)}{\frac{1}{N} \sum_{i=1}^{N} \mathrm{Var}(V_i)} \quad [9]$$

The value $S = 0$ indicates completely asynchronous firing, while $S = 1$ corresponds to fully synchronous network activity. Intermediate values represent intermediate degrees of synchronous firing.

In the case of sliding time bins, this measure is taken by only considering spikes falling into the time window of interest. In Figure 4 we present averages of S over 100 independent realizations, and if a particular run yields a "NaN" result for S at a given time step (indicating no spikes in the associated window), we eliminate that value from the average for that time point (this increases the variability of these values since there are less to average over; thus, this is reflected in an increased range of the $\pm$ STD curves). In

DRAFT

contrast, in Supplementary Figure S2**(b)** we generate a single value the Synchrony Measure (or the other measures of interest) over the last 1000 ms of the simulation. Supplementary Figure S2**(b)** displays this measure averaged over five independent simulations.

Supplementary Figure S2 includes the presentation of our Bifurcation Measure B. This quantifies the presence of sudden and significant changes in the Synchrony Measure over time. First, we take the Synchrony Measure time series for each independent run (i.e., as presented in Figure 3), and use the *smooth* function in MATLAB(58) with a 500 step window, generating a new time series from this moving average filter. This low-pass filter serves to account for fluctuations arising when, for example, a particular 100 ms window includes more or less activity than average. We denote this filtered time-series S_s. Second, we calculate the difference quotient $\frac{\delta S_s}{\delta I}$, where I is the value of the external drive (plotted against time in Figure 3), at each step in the time series. Finally, we take the variance of the values of $\frac{\delta S_s}{\delta I}$ using the *var* function in MATLAB (58): networks in which the Synchrony Measure changes in a consistently linear fashion will have a tight distribution of $\frac{\delta S_s}{\delta I}$ around the average slope (see, for example, Figure 3**(b)**), and thus a low variance; in contrast, networks in which the Synchrony Measure undergoes abrupt transitions will yield a multi-modal distribution of $\frac{\delta S_s}{\delta I}$, with each mode corresponding to different linear sections of S_s, and thus the variance of these values will be notably higher (see, for example, Figure 3**(c)**). The plotted value of B represents an average over the B values calculated for each independent network instantiation. We note that when we calculate the "firing rate Bifurcation Measure" B_e in reference to the four scenarios in Figure 4, we simply replicate the above steps on the firing rate time series rather than the Synchrony Measure time series.

Analysis of FI curves. In Figure 5, we compare activation functions derived from experimental data with model analogues (i.e., the function F described below in Equation 12). In Figure 5**(b)** we show examples of F with epileptogenic and non-epileptogenic levels of heterogeneity alongside samples of the function f (Equation 2) randomly chosen based on the differing heterogeneity levels.

In Figure 5**(a)**, we confirm the correspondence between the F functions and the experimental data by determining the value of σ_e best fitting this data. This process involved three steps: first, we qualitatively determined the portion of the F curves most likely to fit this data as that in $-11.875 \leq U_e \leq -6.25$; second, both the x ($U_e$, [-11.875 -6.25]) and y (probability of firing, [0.003585 .2118]) variables were re-scaled to match the ranges exhibited by the x (input current, pA, [50 250]) and y (firing frequency, Hz, [0 24]) variables in the experimental data; finally, a fit was calculated using MATLAB's (58) Curve Fitting application. This process used a non-linear least squares method, with $r^2 > .93$ for both fits (see details in Results). Additional scaling was performed for plotting so that the two x- and y-axes in Figure 5 remain consistent.

Modeling: Mean-field reduction. Following previous work (34, 38, 69–71) we perform a mean-field reduction of the spiking network in Equation 3. We assume that the firing rate of cells is sufficiently high to make use of the diffusion approximation (72), yielding

$$\alpha_e^{-1}\frac{dU_e}{dt} = -U_e + w_{ee}F(U_e,\sigma_e) + w_{ie}F(U_i,\sigma_i) + I^e \qquad [10]$$

$$\alpha_i^{-1}\frac{dU_i}{dt} = -U_i + w_{ii}F(U_i,\sigma_i) + w_{ei}F(U_e,\sigma_i e) + I^i \qquad [11]$$

where $U_{e,i} = \sum_{j=1}^{N_{e,i}} u_{e,i}^j$ represents the mean activity of the excitatory or inhibitory population, respectively.

The function F represents the average activation function conditioned upon the value of $\sigma_{e,i}$ via the convolution

$$F(U_{e,i},\sigma_{e,i}) = \int_{-\infty}^{\infty} f(U_{e,i}+v,0)\rho(v,\sigma_{e,i})dv \qquad [12]$$

where $\rho(v,\sigma_{e,i}) = N(0,\sigma_{e,i}^2)$ (38, 69, 73).

Linear stability analysis of the mean-field equations. Fixed points $\bar{U}_{e,i}$ of the mean-field equations satisfy

$$0 = -\bar{U_e} + w_{ee}F(\bar{U_e},\sigma_e) + w_{ie}F(\bar{U_i},\sigma_i) + I^e \qquad [13]$$

$$0 = -\bar{U_i} + w_{ii}F(\bar{U_i},\sigma_i) + w_{ei}F(\bar{U_e},\sigma_i e) + I^i \qquad [14]$$

Linearizing about the steady state values of $\bar{U_{e,i}}$ yields the system

$$\mathbf{A}\begin{pmatrix}\delta\bar{U_e}\\ \delta\bar{U_i}\end{pmatrix} = \begin{pmatrix}-1+w_{ee}\alpha_e R^e & w_{ie}\alpha_i R^i\\ w_{ei}\alpha_e R^e & -1+w_{ii}\alpha_i R^i\end{pmatrix}\begin{pmatrix}\delta\bar{U_e}\\ \delta\bar{U_i}\end{pmatrix} \qquad [15]$$

with $R^{e,i} = R(\bar{U}_e,\bar{U}_i) = \int_{\Omega(v)} f'[\bar{U}_{e,i}+v,0]\rho(v,\sigma_{e,i})dv$. The system's stability is given by the eigenvalues of the Jacobian $\mathbf{A}$. Define

$$B = \mathrm{trace}(\mathbf{A}) = -\left(-2 + (w_{ee}\alpha_e)R^e + (w_{ii}\alpha_i)R^i\right) \qquad [16]$$

$$C = \det(\mathbf{A}) = (-1+(w_{ee}\alpha_e)R^e)\left(-1+(w_{ii}\alpha_i)R^i\right) - \left((w_{ie}\alpha_i)R^i\right)\left((w_{ei}\alpha_e)R^e\right) \qquad [17]$$

Eigenvalues of $\mathbf{A}$ are thus given by

$$\lambda_\pm = \frac{-B \pm \sqrt{B^2-4C}}{2} \qquad [18]$$

Bifurcation analysis with varying excitatory input . We investigate bifurcation properties as a function of I^e. In Supplementary Figure S2**(a)**, multi-stability, as denoted by the bold border, is determined by testing for the presence of multiple fixed points at I^e ranging from -15.625:0.625:-6.250, a range encompassing the range for multi-stability shown in Figure 4 (noting $I^e = I_e + I(t)$).

Code Accessibility. The code generating the primary figures is available at https://github.com/Valiantelab/LostNeuralHeterogeneity. Additional code used is available upon request to the authors.

ACKNOWLEDGMENTS. We thank Frances Skinner, Shreejoy Tripathy, Prajay Shah, and Anukrati Nigam for productive intellectual discussions on this topic in the project's early stages. We thank the National Sciences and Engineering Research Council of Canada (NSERC Grants RGPIN-2017-06662 to J.L. and RGPIN-2015-05936 to T.A.V.), the Krembil Foundation (Krembil Seed Grant to J.L. and T.A.V.), the University of Toronto Department of Physiology (Yuet Ngor Wong Award to S.R.), and the Savoy Foundation (Steriade-Savoy Postdoctoral Fellowship to S.R.) for support of this research.

1. EH Reynolds, Introduction: epilepsy in the world. *Epilepsia* **43**, 1–3 (2002).
2. P Jiruska, et al., Synchronization and desynchronization in epilepsy: controversies and hypotheses. *The J. physiology* **591**, 787–797 (2013).
3. HH Jasper, *Jasper's basic mechanisms of the epilepsies.* (OUP USA) Vol. 80, (2012).
4. VK Jirsa, WC Stacey, PP Quilichini, AI Ivanov, C Bernard, On the nature of seizure dynamics. *Brain* **137**, 2210–2230 (2014).
5. ML Saggio, et al., A taxonomy of seizure dynamotypes. *Elife* **9**, e55632 (2020).
6. N Dehghani, et al., Dynamic balance of excitation and inhibition in human and monkey neocortex. *Sci. reports* **6**, 1–12 (2016).
7. J Žiburkus, JR Cressman, SJ Schiff, Seizures as imbalanced up states: excitatory and inhibitory conductances during seizure-like events. *J. neurophysiology* **109**, 1296–1306 (2013).
8. A Renart, et al., The asynchronous state in cortical circuits. *Science* **327**, 587–590 (2010).
9. P Mishra, R Narayanan, Disparate forms of heterogeneities and interactions among them drive channel decorrelation in the dentate gyrus: Degeneracy and dominance. *Hippocampus* **29**, 378–403 (2019).
10. SJ Altschuler, LF Wu, Cellular heterogeneity: do differences make a difference? *Cell* **141**, 559–563 (2010).
11. E Marder, JM Goaillard, Variability, compensation and homeostasis in neuron and network function. *Nat. Rev. Neurosci.* **7**, 563 (2006).
12. K Padmanabhan, NN Urban, Intrinsic biophysical diversity decorrelates neuronal firing while increasing information content. *Nat. neuroscience* **13**, 1276 (2010).
13. SJ Tripathy, K Padmanabhan, RC Gerkin, NN Urban, Intermediate intrinsic diversity enhances neural population coding. *Proc. Natl. Acad. Sci.* **110**, 8248–8253 (2013).
14. Z Zhang, T Valiante, P Carlen, Transition to seizure: from "macro"-to "micro"-mysteries. *Epilepsy research* **97**, 290–299 (2011).
15. AJ Trevelyan, W Bruns, EO Mann, V Crepel, M Scanziani, The information content of physiological and epileptic brain activity. *The J. physiology* **591**, 799–805 (2013).

DRAFT

16. R Cossart, et al., Dendritic but not somatic gabaergic inhibition is decreased in experimental epilepsy. *Nat. neuroscience* **4**, 52–62 (2001).
17. I Cobos, et al., Mice lacking dlx1 show subtype-specific loss of interneurons, reduced inhibition and epilepsy. *Nat. neuroscience* **8**, 1059–1068 (2005).
18. EC Arnold, C McMurray, R Gray, D Johnston, Epilepsy-induced reduction in hcn channel expression contributes to an increased excitability in dorsal, but not ventral, hippocampal ca1 neurons. *Eneuro* **6** (2019).
19. A Klaassen, et al., Seizures and enhanced cortical gabaergic inhibition in two mouse models of human autosomal dominant nocturnal frontal lobe epilepsy. *PNAS* **103**, 19152–19157 (2006).
20. AJ Albertson, J Yang, JJ Hablitz, Decreased hyperpolarization-activated currents in layer 5 pyramidal neurons enhances excitability in focal cortical dysplasia. *J. neurophysiology* **106**, 2189–2200 (2011).
21. TP Sutula, FE Dudek, Unmasking recurrent excitation generated by mossy fiber sprouting in the epileptic dentate gyrus: an emergent property of a complex system. *Prog. brain research* **163**, 541–563 (2007).
22. HM Chameh, et al., Diversity amongst human cortical pyramidal neurons revealed via their sag currents and frequency preferences. *Nat. Commun.* **12** (2021).
23. RD Hodge, et al., Conserved cell types with divergent features in human versus mouse cortex. *Nature* **573**, 61–68 (2019).
24. L Beaulieu-Laroche, et al., Enhanced dendritic compartmentalization in human cortical neurons. *Cell* **175**, 643–651 (2018).
25. B Kalmbach, et al., Signature morpho-electric, transcriptomic, and dendritic properties of extratelencephalic-projecting human layer 5 neocortical pyramidal neurons. *bioRxiv* **Preprint** (2020).
26. BW Colder, RC Frysinger, CL Wilson, RM Harper, J Engel Jr, Decreased neuronal burst discharge near site of seizure onset in epileptic human temporal lobes. *Epilepsia* **37**, 113–121 (1996).
27. PA Schwartzkroin, DA Turner, WD Knowles, AR Wyler, Studies of human and monkey "epileptic" neocortex in the in vitro slice preparation. *Annals Neurol. Off. J. Am. Neurol. Assoc. Child Neurol. Soc.* **13**, 249–257 (1983).
28. MA Kramer, HE Kirsch, AJ Szeri, Pathological pattern formation and cortical propagation of epileptic seizures. *J. Royal Soc. Interface* **2**, 113–127 (2005).
29. TP Vogels, L Abbott, Gating multiple signals through detailed balance of excitation and inhibition in spiking networks. *Nat. neuroscience* **12**, 483 (2009).
30. S Ostojic, Two types of asynchronous activity in networks of excitatory and inhibitory spiking neurons. *Nat. neuroscience* **17**, 594–600 (2014).
31. MP Jadi, TJ Sejnowski, Cortical oscillations arise from contextual interactions that regulate sparse coding. *Proc. Natl. Acad. Sci.* **111**, 6780–6785 (2014).
32. MP Jadi, TJ Sejnowski, Regulating cortical oscillations in an inhibition-stabilized network. *Proc. IEEE* **102**, 830–842 (2014).
33. GT Neske, SL Patrick, BW Connors, Contributions of diverse excitatory and inhibitory neurons to recurrent network activity in cerebral cortex. *J. Neurosci.* **35**, 1089–1105 (2015).
34. S Rich, A Hutt, FK Skinner, TA Valiante, J Lefebvre, Neurostimulation stabilizes spiking neural networks by disrupting seizure-like oscillatory transitions. *Sci. reports* **10**, 1–17 (2020).
35. SN Chow, JK Hale, *Methods of bifurcation theory*. (Springer Science & Business Media) Vol. 251, (2012).
36. RP Boland, T Galla, AJ McKane, How limit cycles and quasi-cycles are related in systems with intrinsic noise. *J. Stat. Mech. Theory Exp.* **2008**, P09001 (2008).
37. JF Mejias, A Longtin, Differential effects of excitatory and inhibitory heterogeneity on the gain and asynchronous state of sparse cortical networks. *Front. computational neuroscience* **8**, 107 (2014).
38. J Lefebvre, A Hutt, JF Knebel, K Whittingstall, MM Murray, Stimulus statistics shape oscillations in nonlinear recurrent neural networks. *J. Neurosci.* **35**, 2895–2903 (2015).
39. C Börgers, N Kopell, Synchronization in networks of excitatory and inhibitory neurons with sparse, random connectivity. *Neural computation* **15**, 509–538 (2003).
40. C Börgers, N Kopell, Effects of noisy drive on rhythms in networks of excitatory and inhibitory neurons. *Neural computation* **17**, 557–608 (2005).
41. C Börgers, GT Franzesi, FE LeBeau, ES Boyden, NJ Kopell, Minimal size of cell assemblies coordinated by gamma oscillations. *PLoS Comput. Biol* **8**, e1002362 (2012).
42. MY Yim, A Aertsen, S Rotter, Impact of intrinsic biophysical diversity on the activity of spiking neurons. *Phys. Rev. E* **87**, 032710 (2013).
43. J Mejias, A Longtin, Optimal heterogeneity for coding in spiking neural networks. *Phys. Rev. Lett.* **108**, 228102 (2012).
44. R Cossart, The maturation of cortical interneuron diversity: how multiple developmental journeys shape the emergence of proper network function. *Curr. opinion neurobiology* **21**, 160–168 (2011).
45. ZJ Huang, A Paul, The diversity of gabaergic neurons and neural communication elements. *Nat. Rev. Neurosci.* **20**, 563–572 (2019).
46. C Gavrilovici, E Pollock, M Everest, MO Poulter, The loss of interneuron functional diversity in the piriform cortex after induction of experimental epilepsy. *Neurobiol. disease* **48**, 317–328 (2012).
47. N Niu, et al., Performance of pet imaging for the localization of epileptogenic zone in patients with epilepsy: a meta-analysis. *Eur. Radiol.* **31**, 1–14 (2021).
48. B Frauscher, et al., High-frequency oscillations: the state of clinical research. *Epilepsia* **58**, 1316–1329 (2017).
49. P Jiruska, et al., Update on the mechanisms and roles of high-frequency oscillations in seizures and epileptic disorders. *Epilepsia* **58**, 1330–1339 (2017).
50. RF Ackermann, DM Finch, TL Babb, J Engel, Increased glucose metabolism during long-duration recurrent inhibition of hippocampal pyramidal cells. *J. Neurosci.* **4**, 251–264 (1984).
51. S Rich, H Moradi Chameh, V Sekulic, TA Valiante, FK Skinner, Modeling reveals human–rodent differences in h-current kinetics influencing resonance in cortical layer 5 neurons. *Cereb. Cortex* **31**, 845–872 (2021).
52. SA Lee, DD Spencer, SS Spencer, Intracranial eeg seizure-onset patterns in neocortical epilepsy. *Epilepsia* **41**, 297–307 (2000).
53. AL Velascol, CL Wilson, TL Babb, J Engel Jr, Functional and anatomic correlates of two frequently observed temporal lobe seizure-onset patterns. *Neural plasticity* **7**, 49–63 (1999).
54. E Marder, Variability, compensation, and modulation in neurons and circuits. *Proc. Natl. Acad. Sci. United States Am.* **108 Suppl 3**, 15542–15548 (2011).
55. A Fallah, et al., Anterior cervical discectomy with arthroplasty versus arthrodesis for single-level cervical spondylosis: a systematic review and meta-analysis. *PLoS One* **7**, e43407 (2012).
56. G Kostopoulos, C Drapeau, M Avoli, A Olivier, JG Villemeure, Endogenous adenosine can reduce epileptiform activity in the human epileptogenic cortex maintained in vitro. *Neurosci. letters* **106**, 119–124 (1989).
57. BE Kalmbach, et al., h-channels contribute to divergent intrinsic membrane properties of supragranular pyramidal neurons in human versus mouse cerebral cortex. *Neuron* **100**, 1194–1208 (2018).
58. MATLAB, *version 9.6.0 (R2019a)*. (The MathWorks Inc., Natick, Massachusetts), (2019).
59. DL Snyder, MI Miller, *Random point processes in time and space*. (Springer Science & Business Media), (2012).
60. CF Stevens, AM Zador, When is an integrate-and-fire neuron like a poisson neuron? in *Advances in neural information processing systems*. pp. 103–109 (1996).
61. RD Traub, JG Jefferys, MA Whittington, Simulation of gamma rhythms in networks of interneurons and pyramidal cells. *J. computational neuroscience* **4**, 141–150 (1997).
62. S Rich, M Zochowski, V Booth, Dichotomous dynamics in ei networks with strongly and weakly intra-connected inhibitory neurons. *Front. neural circuits* **11**, 104 (2017).
63. S Rich, M Zochowski, V Booth, Effects of neuromodulation on excitatory–inhibitory neural network dynamics depend on network connectivity structure. *J. Nonlinear Sci.* **30**, 1–24 (2018).
64. E Golder, J Settle, The box-müller method for generating pseudo-random normal deviates. *J. Royal Stat. Soc. Ser. C (Applied Stat.* **25**, 12–20 (1976).
65. D Golomb, J Rinzel, Dynamics of globally coupled inhibitory neurons with heterogeneity. *Phys. review E* **48**, 4810 (1993).
66. D Golomb, J Rinzel, Clustering in globally coupled inhibitory neurons. *Phys. D: Nonlinear Phenom.* **72**, 259–282 (1994).
67. S Rich, V Booth, M Zochowski, Intrinsic cellular properties and connectivity density determine variable clustering patterns in randomly connected inhibitory neural networks. *Front. neural circuits* **10**, 82 (2016).
68. S Rich, et al., Inhibitory network bistability explains increased interneuronal activity prior to seizure onset. *Front. Neural Circuits* **13**, 81 (2020).
69. A Hutt, A Mierau, J Lefebvre, Dynamic control of synchronous activity in networks of spiking neurons. *PloS one* **11** (2016).
70. RA Stefanescu, R Shivakeshavan, SS Talathi, Computational models of epilepsy. *Seizure* **21**, 748–759 (2012).
71. A Hutt, J Lefebvre, D Hight, HA Kaiser, Phase coherence induced by additive gaussian and non-gaussian noise in excitable networks with application to burst suppression-like brain signals. *Front. applied mathematics statistics* **5**, 69 (2020).
72. B Gluss, A model for neuron firing with exponential decay of potential resulting in diffusion equations for probability density. *Bull. Math. Biophys.* **29**, 233–243 (1967).
73. A Hutt, J Lefebvre, D Hight, J Sleigh, Suppression of underlying neuronal fluctuations mediates EEG slowing during general anaesthesia. *Neuroimage* **179**, 414–428 (2018).

DRAFT

PNAS
www.pnas.org

Supplementary Information for

Resilience through diversity: Lost neuronal heterogeneity in human epilepsy renders networks vulnerable to synchronous transitions

Scott Rich, Homeira Moradi Chameh, Jeremie Lefebvre, Taufik A. Valiante

Scott Rich, scott.rich@uhnresearch.ca

This PDF file includes:

Figs. S1 to S6 (not allowed for Brief Reports)

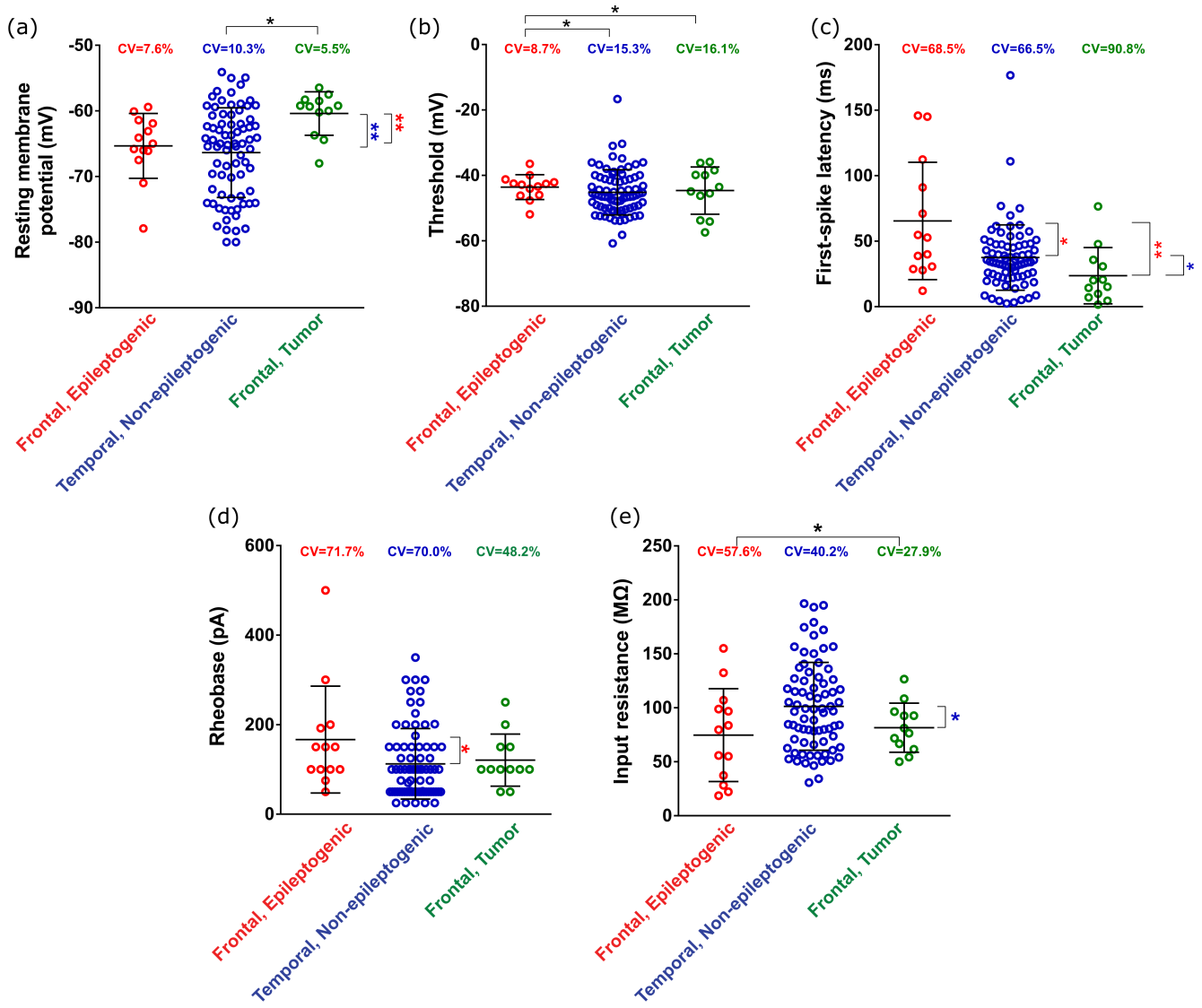

Fig. S1. Details from electrophysiological recordings. **(a)**: Distribution of resting membrane potentials (RMP) in our three neuronal populations. None of the distributions are deemed normal after failing the D'Agostino and Pearson omnibus, Shapiro-Wilk, and Kolmogorof-Smirnov normality tests with alpha=0.05. Mean RMP is significantly increased in the frontal, tumor (n=12) population compared to both the frontal, epileptogenic (n=13; p=0.003; Non-parameteric Mann-Whitney test) and temporal, non-epileptogenic (n=77; p=0.002) populations. Coefficient of variation (CV) of these populations is significantly increased in the temporal, non-epileptogenic population compared to the frontal, tumor population (p=0.03; two sample coefficient of variation test). Plotted bars indicate mean $\pm$ standard deviation (SD). **(b)**: Distribution of threshold voltages in our three neuronal populations. All three distributions are deemed normal after passing the Kolmogorof-Smirnov normality test with alpha=0.05. No significant differences between mean threshold voltages were observed across all three populations (unpaired t test with Welch's correction). The CV of the threshold voltage in the frontal, epileptogenic population was significantly lower than in the temporal, non-epileptogenic population (p=0.04; two sample coefficient of variation test) and than in the frontal, tumor population (p=0.04). Plotted bars indicate mean $\pm$ SD. **(c)** Distribution of first-spike latencies (time between stimulus application and first spike) in our three neuronal populations. None of the distributions are deemed normal after failing the D'Agostino and Pearson omnibus, Shapiro-Wilk, and Kolmogorof-Smirnov normality tests with alpha=0.05. Mean latency is significantly lower in the temporal, non-epileptogenic population compared to the frontal, epileptogenic population (p=0.03; Non-parametric Mann-Whitney test), and mean latency is significantly lower in the frontal, tumor population compared to both the frontal, epileptogenic (p=0.0045) and temporal, non-epileptogenic (p=0.02) populations. No significant differences were observed between the CVs of these populations. Plotted bars indicate mean $\pm$ SD. **(d)** Distribution of rheobases (minimal input current required to elicit first spike) in our three neuronal populations. None of the distributions are deemed normal after failing the D'Agostino and Pearson omnibus, Shapiro-Wilk, and Kolmogorof-Smirnov normality tests with alpha=0.05. The mean rheobase of the temporal, non-epileptogenic population is significantly lower compared to the frontal, epileptogenic population (p=0.045; Non-parametric Mann-Whitney test). No significant differences were observed between the CVs of these populations. Plotted bars indicate mean $\pm$ SD. **(e)** Distribution of input resistances in our three neuronal populations. All three distributions are deemed normal after passing the D'Agostino and Pearson omnibus, Shapiro-Wilk, and Kolmogorof-Smirnov normality tests with alpha=0.05. Mean input resistance of the frontal, tumor population is significantly lower compared to the temporal, non-epileptogenic population (p=0.02; Unpaired t-test with Welch's correction). The CV of the frontal, tumor population was significantly lower compared to the frontal, epileptogenic population (p=0.047; two-sampled coefficient of variation test). Plotted bars indicate mean $\pm$ SD.

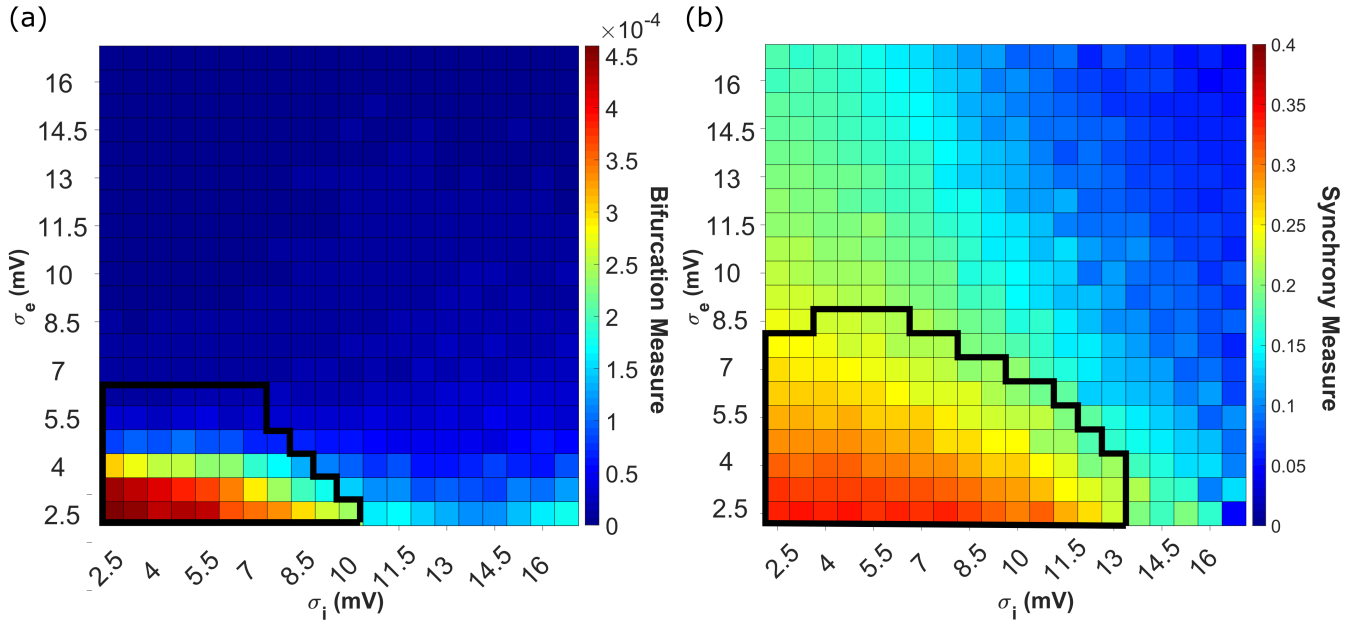

Fig. S2. Exploration of a larger σ_e and σ_i parameter space highlights the asymmetric effects of excitatory and inhibitory heterogeneity on sudden transitions into synchrony. **(a)**: Visualization quantifying the tendency for spiking networks to undergo a sudden and notable increase in excitatory synchrony over time, when subjected to a linearly increasing input as in Figures 2, 3, and 4 (but over 2048 as opposed to 2500 ms), via the Bifurcation Measure B. Results are shown averaged over 10 independent simulations. Bolded region demarcates networks whose mean-field analogues exhibit any multi-stability from those that do not (remainder of heatmap). **(b)**: Dynamics of spiking networks with a constant external input ($I(t) = 15.625$) where either synchronous or asynchronous activity can arise. The excitatory synchrony is quantified via the Synchrony Measure taken over the final 1000 ms of a 2048 ms simulation, and the presented value is averaged over five independent simulations. The bolded region demarcates networks whose mean-field analogues have an unstable oscillator from those that have a stable oscillator (remainder of heatmap) as their lone fixed point when $I(t) = 15.625$.

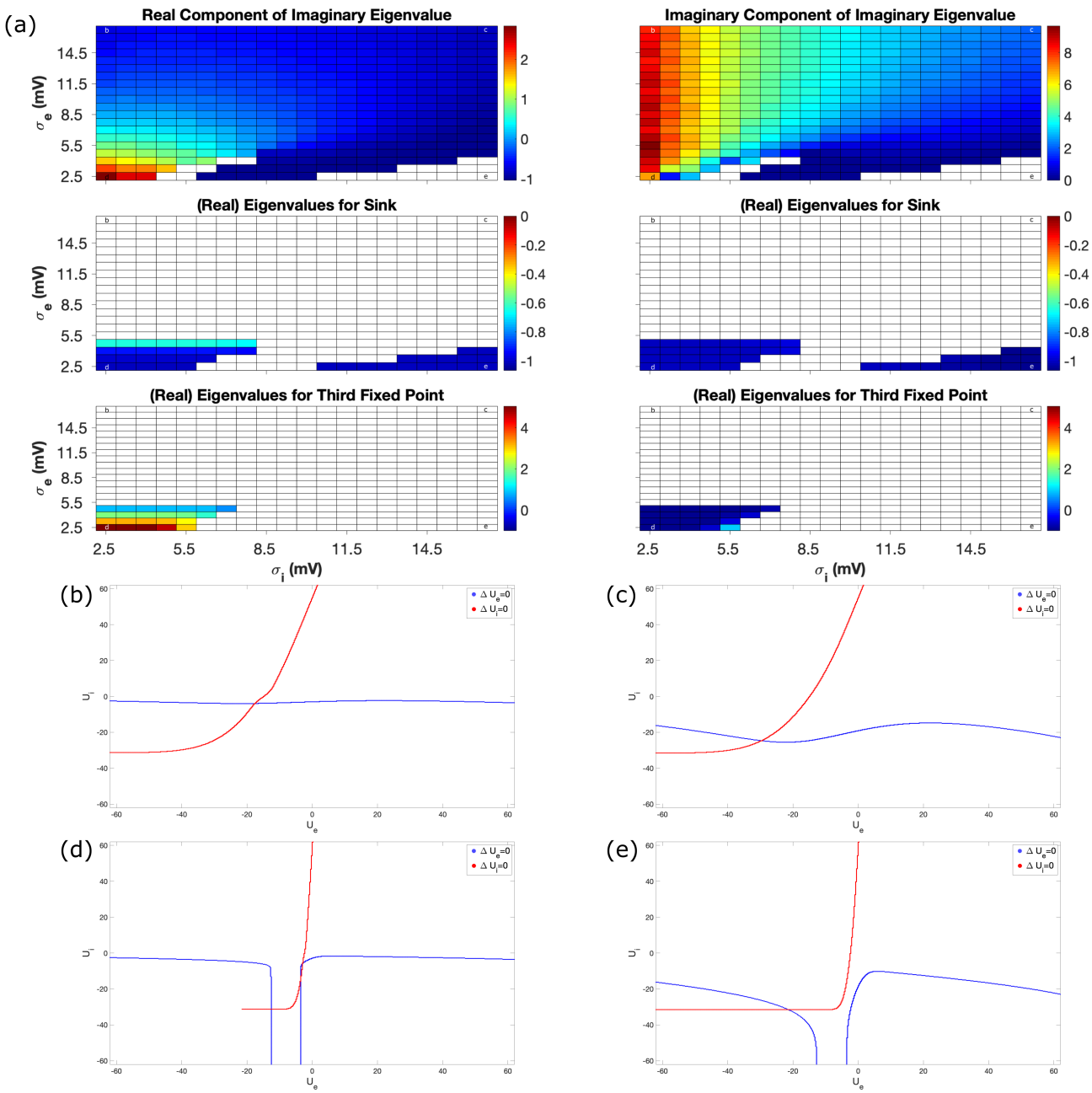

Fig. S3. Fixed points and eigenvalues of mean-field equations for $I(t) = 3.125$. (a): The mean-field system with this $I(t)$ value can yield multiple fixed points: we calculate their eigenvalues, sort them by their classifications, and visualize these eigenvalues via heatmaps. In this example, we see that multiple fixed points arise only when both σ_e and σ_i are low (i.e. the bottom-left of the heatmap). **(b-e)**: Fixed points are determined by finding the intersections of the U_e and U_i nullclines, visualized for the corners of our heatmap (top-left in panel **(b)**, top-right in panel **(c)**, bottom-left in panel **(d)**, and bottom-right in panel **(e)**). Multiple fixed points correspond with multiple intersections of these curves, as seen exclusively in panel **(d)**.

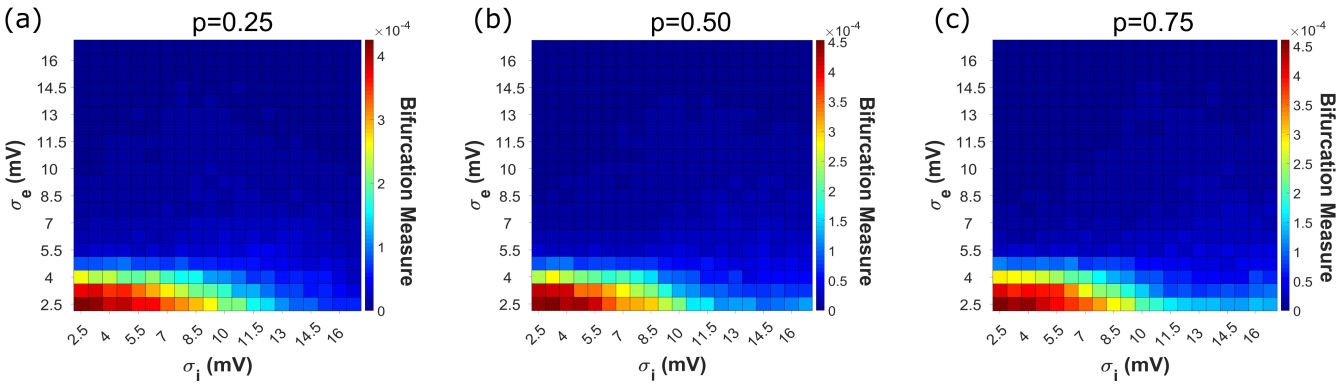

Fig. S4. Dynamics of spiking networks are robust to more sparse connectivity paradigms. Bifurcation Measure B pattern over our parameter space remains similar with $p = 0.25$ (panel **(a)**), $p = 0.50$ (panel **(b)**), and $p = 0.75$ (panel **(c)**), when compared to the case of $p = 1.00$ seen in Figure S2**(a)**. In each case the "asymmetry" in the effects of σ_e and σ_i is preserved. Heatmaps present results averaged over ten independent simulations.

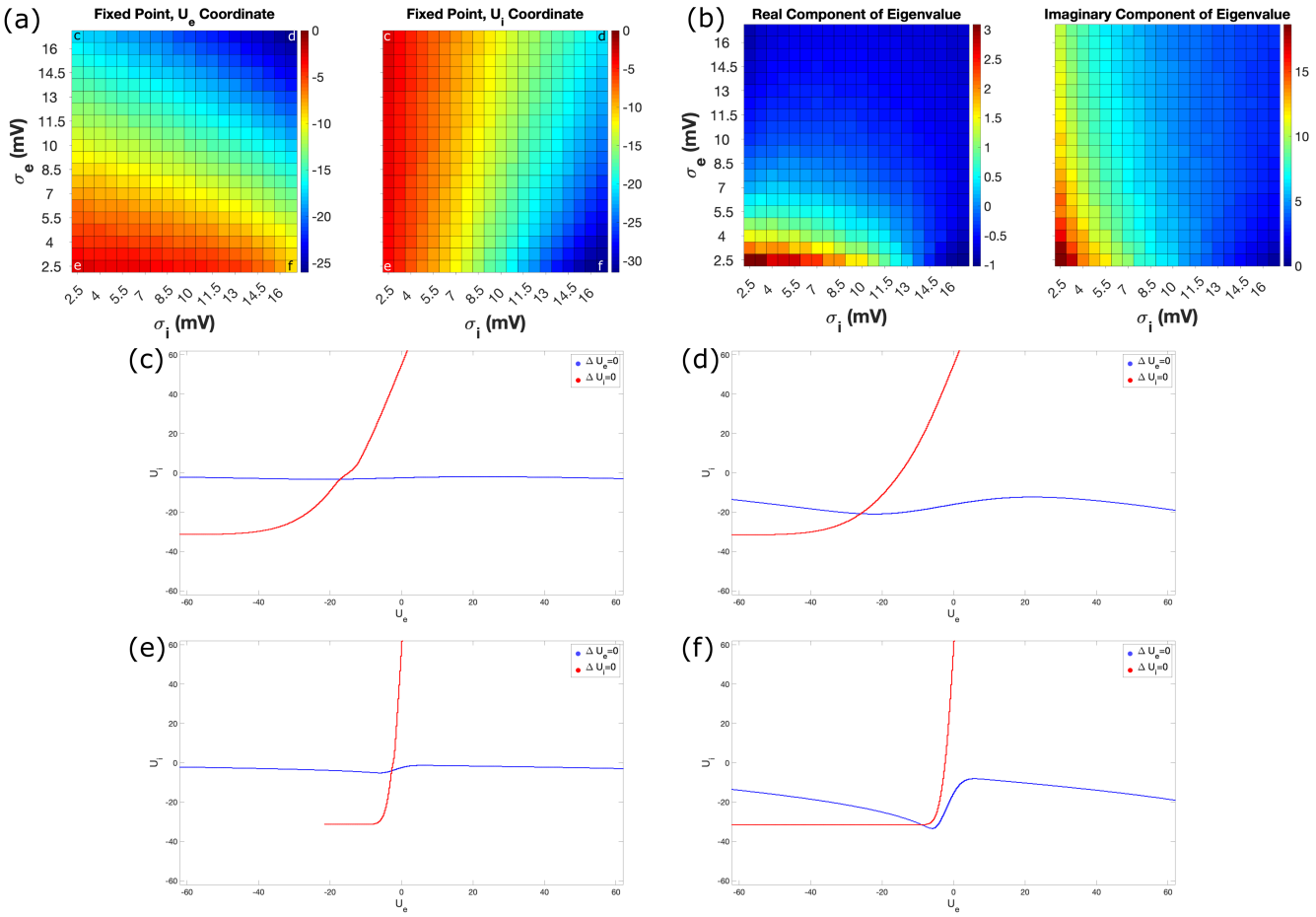

Fig. S5. Fixed points and eigenvalues of mean-field equations for $I(t) = 15.625$. (a): As all mean-field systems in our parameter space yield a single fixed point when $I(t) = 15.625$, we visualize the U_e and U_i coordinates of this fixed point using a heatmap. **(b)**: Each fixed point has imaginary eigenvalues, which we visualize by plotting the real and imaginary components of the eigenvalue associated with the fixed point in a heatmap. **(c-f)**: Fixed points are determined by finding the intersections of the U_e and U_i nullclines, visualized for the corners of our heatmap (top-left in panel **(c)**, top-right in panel **(d)**, bottom-left in panel **(e)**, and bottom-right in panel **(f)**).

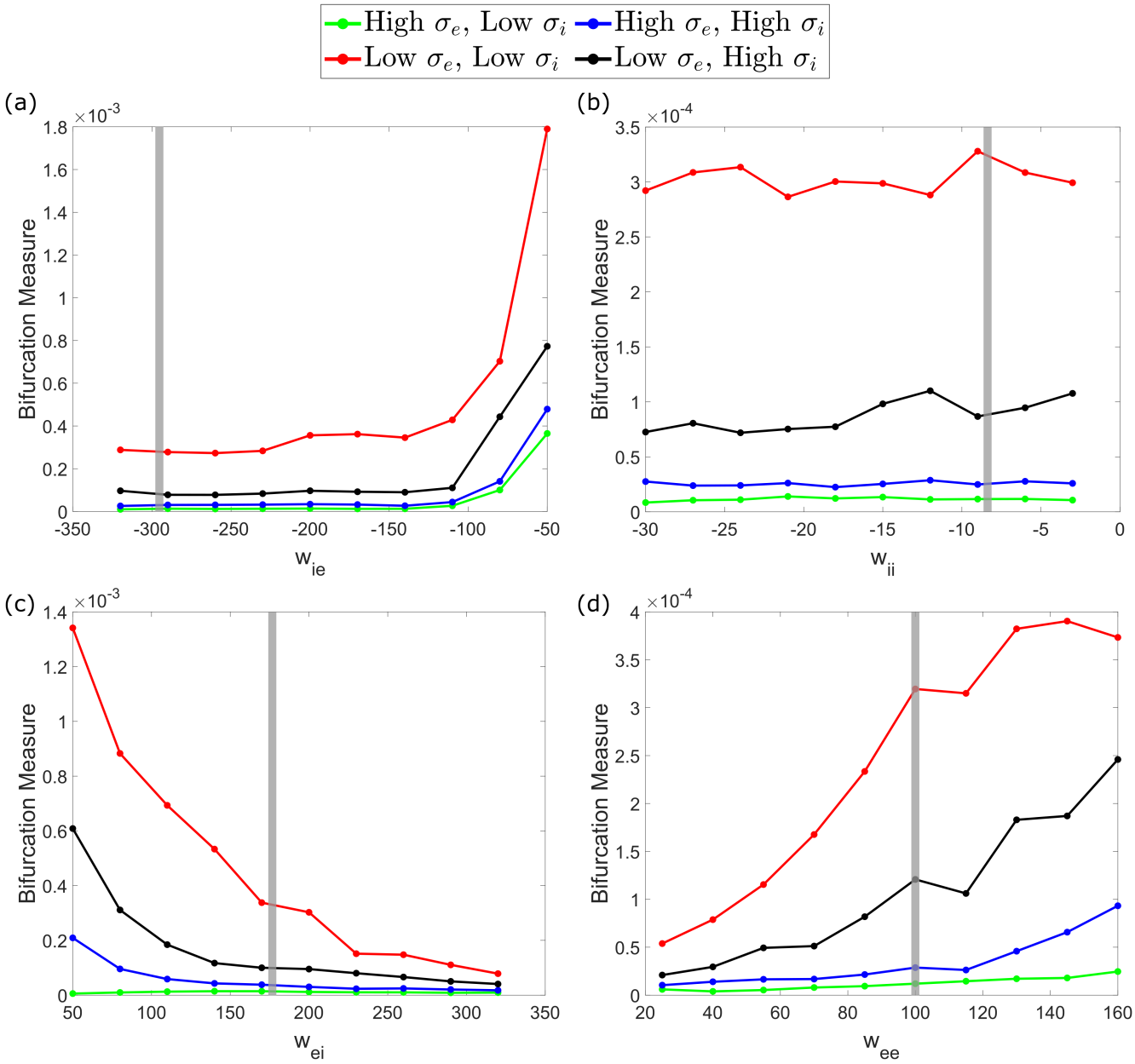

Fig. S6. Network dynamics are robust to a range of synaptic weights. (a-d): Examination of changes to network dynamics, as quantified via the Bifurcation Measure, caused by varying a single synaptic weight (w_{ie} in **(a)**, w_{ii} in **(b)**, w_{ei} in **(c)**, and w_{ee} in **(d)**). Vertical grey bar represents the default value of the synaptic weight as given in Table 1. Values of high/low heterogeneity correspond with those used in exemplar networks in Figures 3 and 4. The Bifurcation Measure is always highest when both σ_e and σ_i are low (red trace), and the other traces (each representing a scenario where at least one of σ_e or σ_i is high) rarely exceed the default Bifurcation Measure of the low σ_e and σ_i case (approximately $3\text{x}10^{-4}$). This indicates "sudden transitions" into synchronous dynamics on the magnitude of that seen in Figure 3**(c)** and Figure 4**(c)** occur preferentially in the case of both low σ_e and σ_i, even for variations on the chosen synaptic weights. The preserved relationship between the four scenarios represented by the different traces (low σ_e and low σ_i always yielding the highest bifurcation measure, followed by low σ_e and high σ_i, followed then by very similar values in both high σ_e scenarios) is further evidence of the robustness of the patterns observed in the results of Figures 3 and 4. Each data point represents an average over 10 independent simulations.